Science Advances
AAAS

Supplementary Materials for

Porous liquid metal–elastomer composites with high leakage resistance and antimicrobial property for skin-interfaced bioelectronics

Yadong Xu *et al.*

Corresponding author: Zheng Yan, yanzheng@missouri.edu; Jingwei Xie, jingwei.xie@unmc.edu; Guoliang Huang, huangg@missouri.ed

Sci. Adv. **9**, eadf0575 (2023)
DOI: 10.1126/sciadv.adf0575

The PDF file includes:

Other Supplementary Material for this manuscript includes the following:

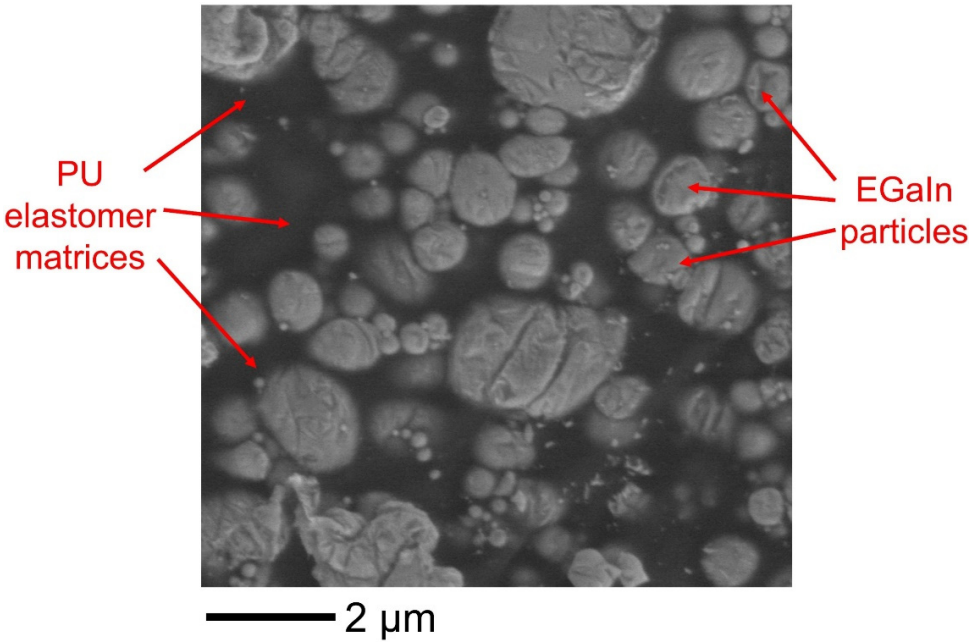

Figure S1. SEM image of nonporous EGaIn composites before mechanical sintering. Here, PU is used as elastomer matrices.

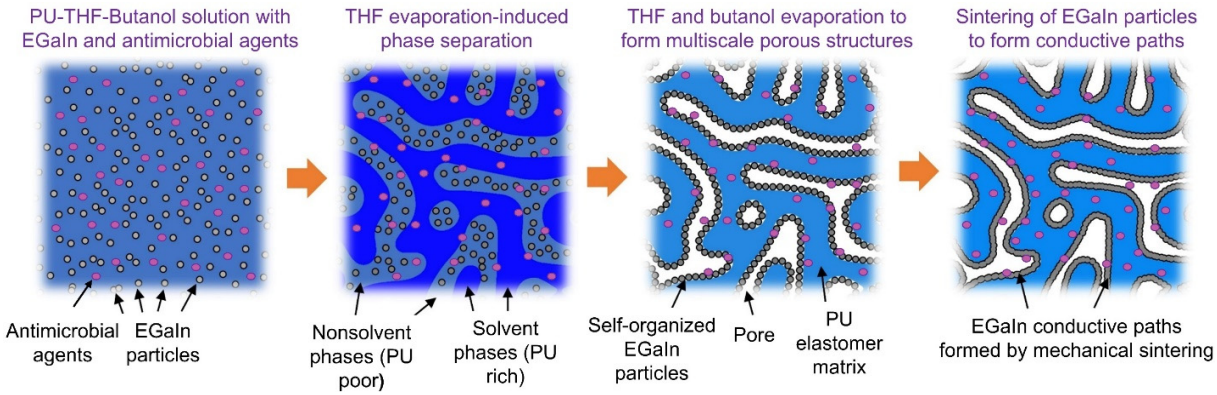

Figure S2. Schematic of phase-separation-based synthesis of multifunctional porous EGaIn composites. First, a precursor solution, comprising PU, THF (solvent), 1-butanol (nonsolvent), EGaIn particles and antimicrobial agents (i.e., BEHS modified ε-PL), is prepared. Multiscale porous structures are induced by phase separation due to sequential evaporation of THF (boiling point: 66 °C) and 1-butanol (boiling point: 117.7 °C). During phase separation, EGaIn particles self-organize on pore surfaces due to the Pickering effect (i.e., the segregation of colloidal particles to the interface between two fluids to minimize the free energy of the system). Finally, mechanical sintering process is employed to collapse self-organized EGaIn particles to form conductive paths.

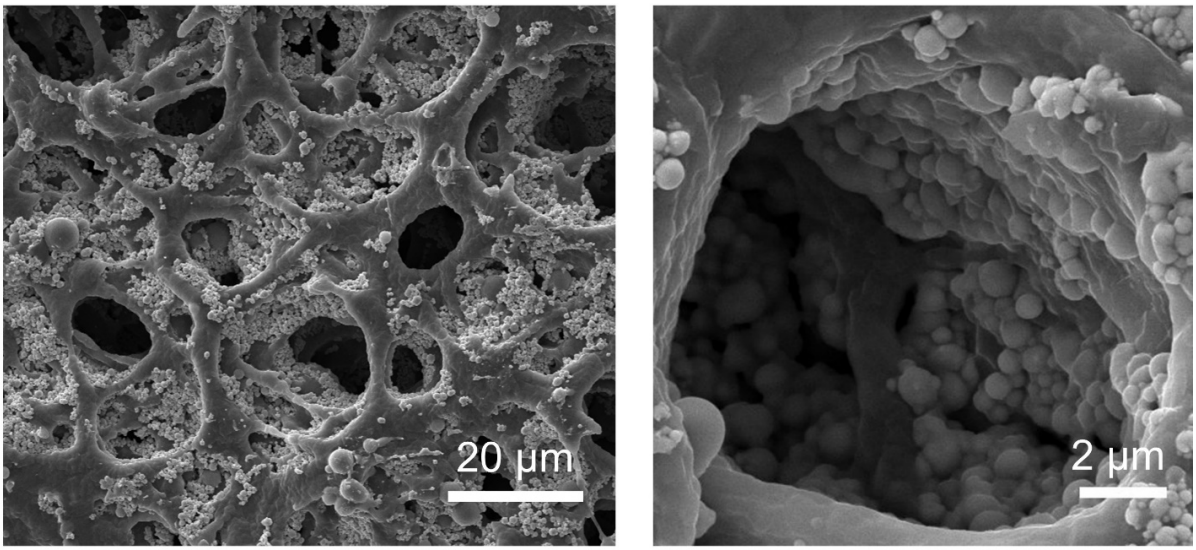

Figure S3. SEM images of porous EGaIn composites before sintering. SEM characterizations clearly indicate that EGaIn particles self-organize on the surfaces of porous structures.

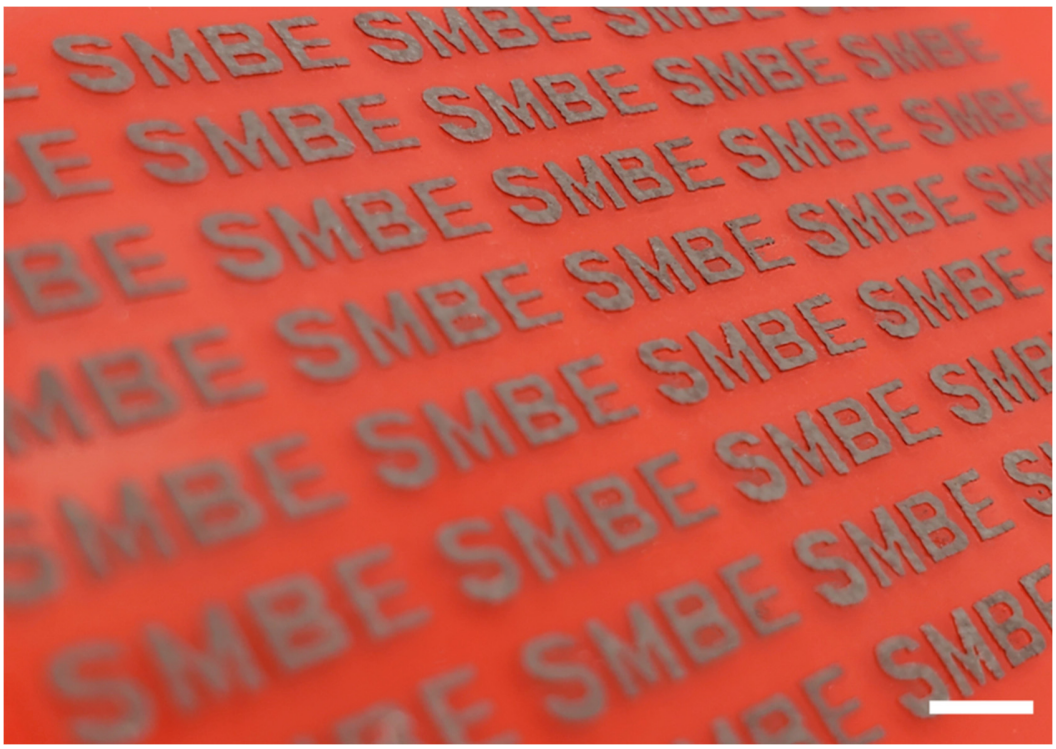

Figure S4. Optical image of an array of SMBE letters, made of porous EGaIn composites, fabricated using a CO_2 laser system. This image indicates scalability and high reproducibility of the laser-assisted fabrication process. Here, a VLS2.30 universal CO_2 laser system is adopted for patterning porous EGaIn composites. Scale bar: 5 mm.

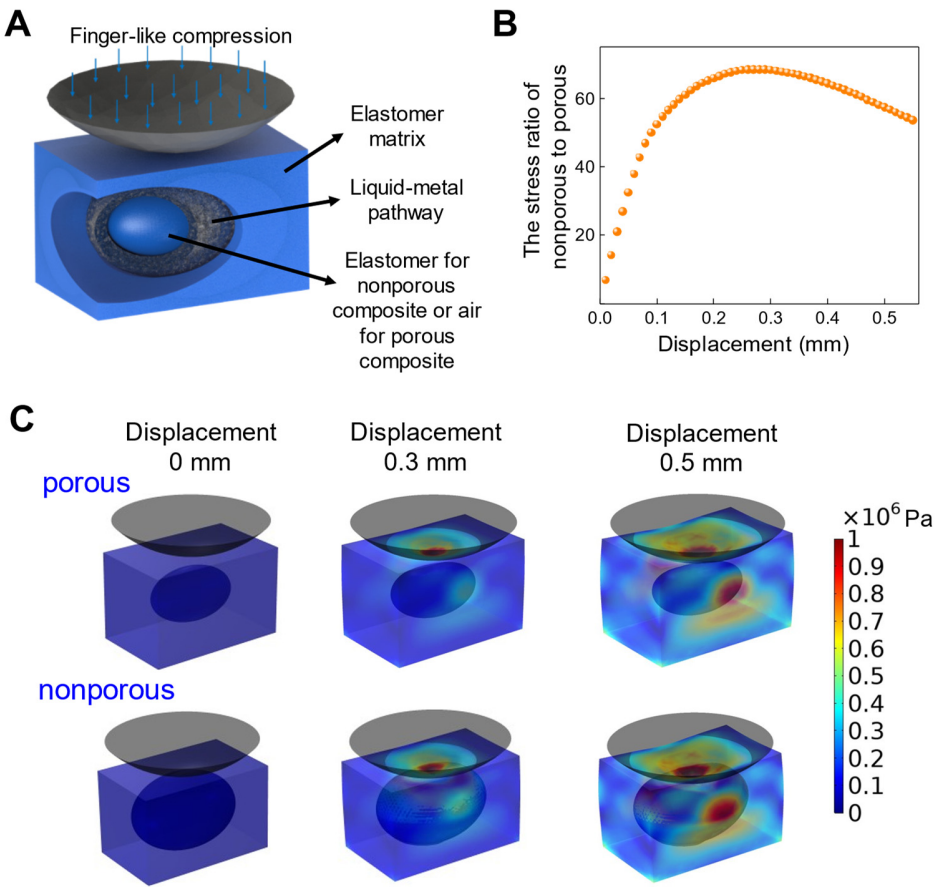

Figure S5. FEA simulations of nonporous and porous EGaIn composites upon mechanical compression. A, Schematic illustration of the simplified structural model used for FEA simulations. **B**, The ratio of the average stress on EGaIn pathways in nonporous and porous composites as a function of the applied displacement, showing significantly lower average stresses on EGaIn pathways in porous composites due to damping effects of porous structures. **C**, FEA simulations for the distributions of von Mises stresses in porous (top) and nonporous (bottom) EGaIn composites under finger-like compressions.

Here, to theoretically study the leakage resistance of EGaIn composites under mechanical loading, FEA simulations were performed in COMOSL-Multiphysics using the solid-mechanics model with the stationary analysis. A 3D model for the simulation is given in (**A**), where a sandwich structure was adopted. Specifically, EGaIn pathways were sandwiched between the PU matrix and air (i.e., solid-air interface) in porous composites and the PU matrix in nonporous composites (i.e., solid-solid interface). The dimension for the PU rectangular block is 8×5×5 mm. The dimension for the ellipsoidal EGaIn path is 3.2×2.2×2.2 mm. A rigid circular shell with contact boundary conditions was employed to apply compression. Notably, when EGaIn composites subjected to compressive loads, the average stress on the EGaIn path was considerably reduced in the porous composite as compared to that of the nonporous composite (**B, C**) due to damping effects.

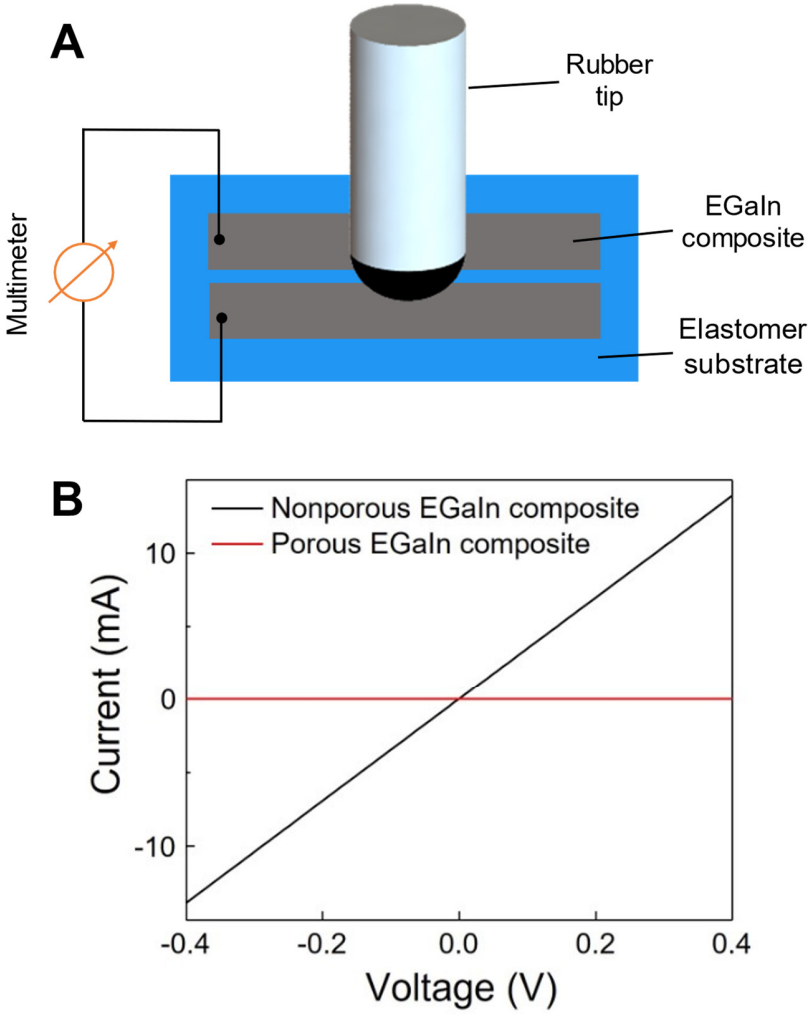

Figure S6. Compression tests of conductive traces of nonporous and porous EGaIn composites. A, Schematic illustration of the setup used for compression tests. **B**, I-V curves of the neighboring conductive traces of nonporous (black) and porous (red) composites after repetitive compression (0.4 MPa for 100 cycles), indicating the adjacent conductive traces of nonporous EGaIn composites were shorting due to liquid-metal leakage.

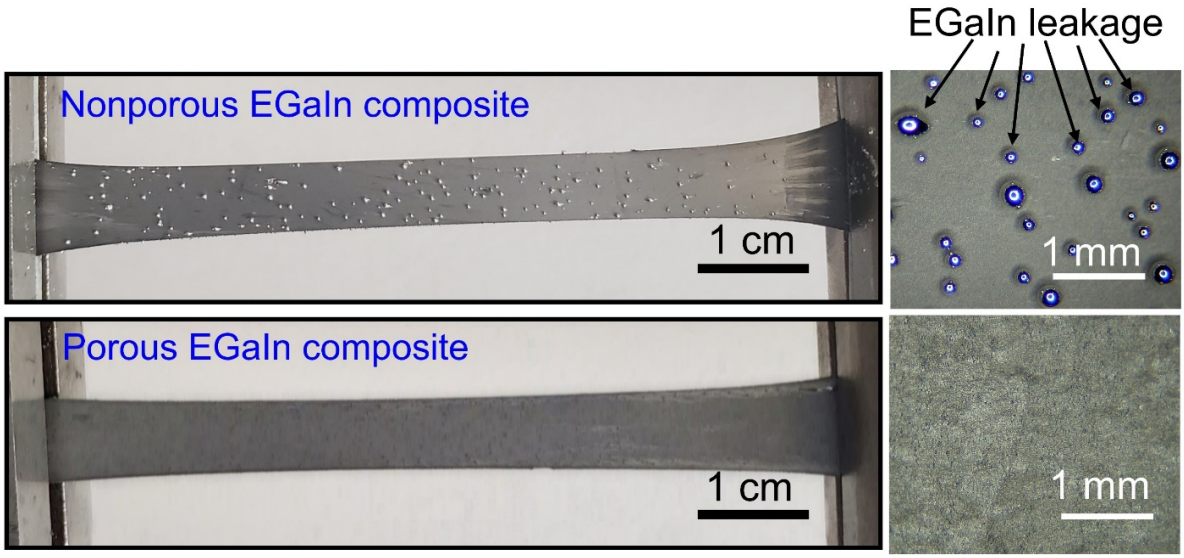

Figure S7. Optical images of cyclic stretching tests (400% strain, 100 cycles) of nonporous and porous EGaIn composites. Severe liquid-metal droplet leakage is observed on the surface of the nonporous EGaIn composite (top). And liquid metal droplet leakage is hardly seen on the porous EGaIn composite (bottom), which has the same electrical conductivity with that of the nonporous EGaIn composite.

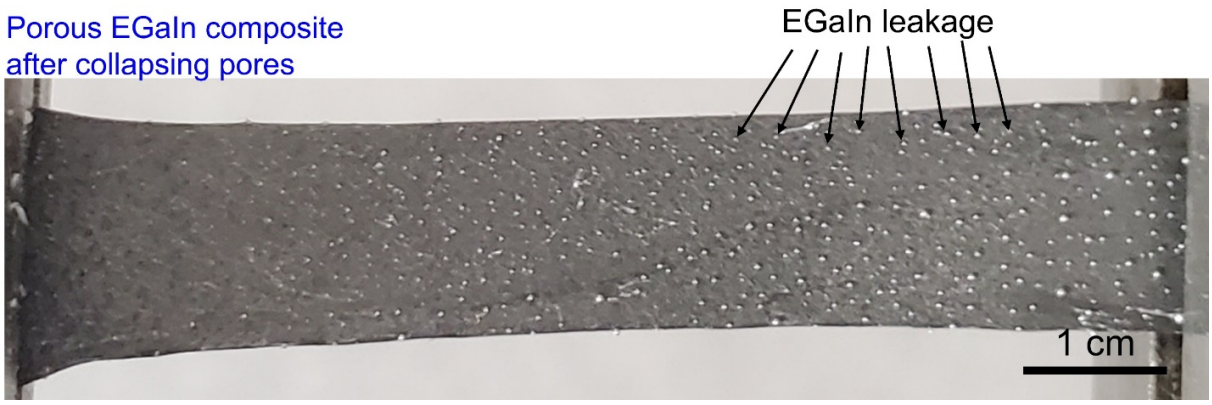

Figure S8. Optical image of the porous EGaIn composite under stretching (300% strain) after its porous structures were collapsed using dimethylformamide vapor. Here, evident EGaIn droplet leakage was seen under stretching after collapsed porous structures, further confirming the critical role of porous geometries in enabling outstanding leakage-resistance.

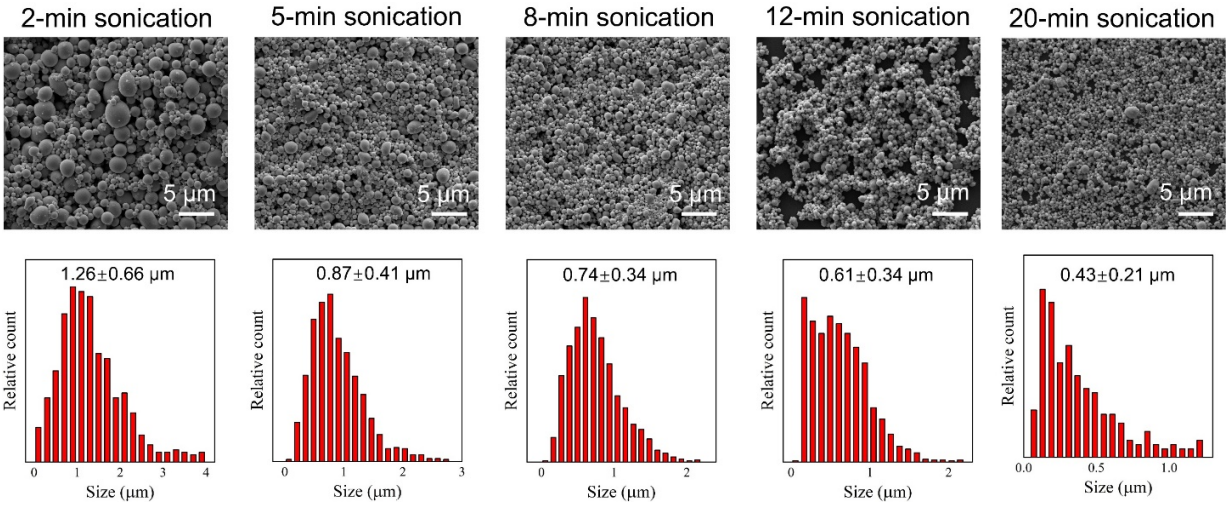

Figure S9. Preparation of EGaIn particles by tip sonication. SEM images (top) and particle size analysis (bottom) of EGaIn particles obtained with 2, 5, 8, 12 and 20 mins of tip sonication (50% amplitude) of bulk EGaIn in 1-butanol solution.

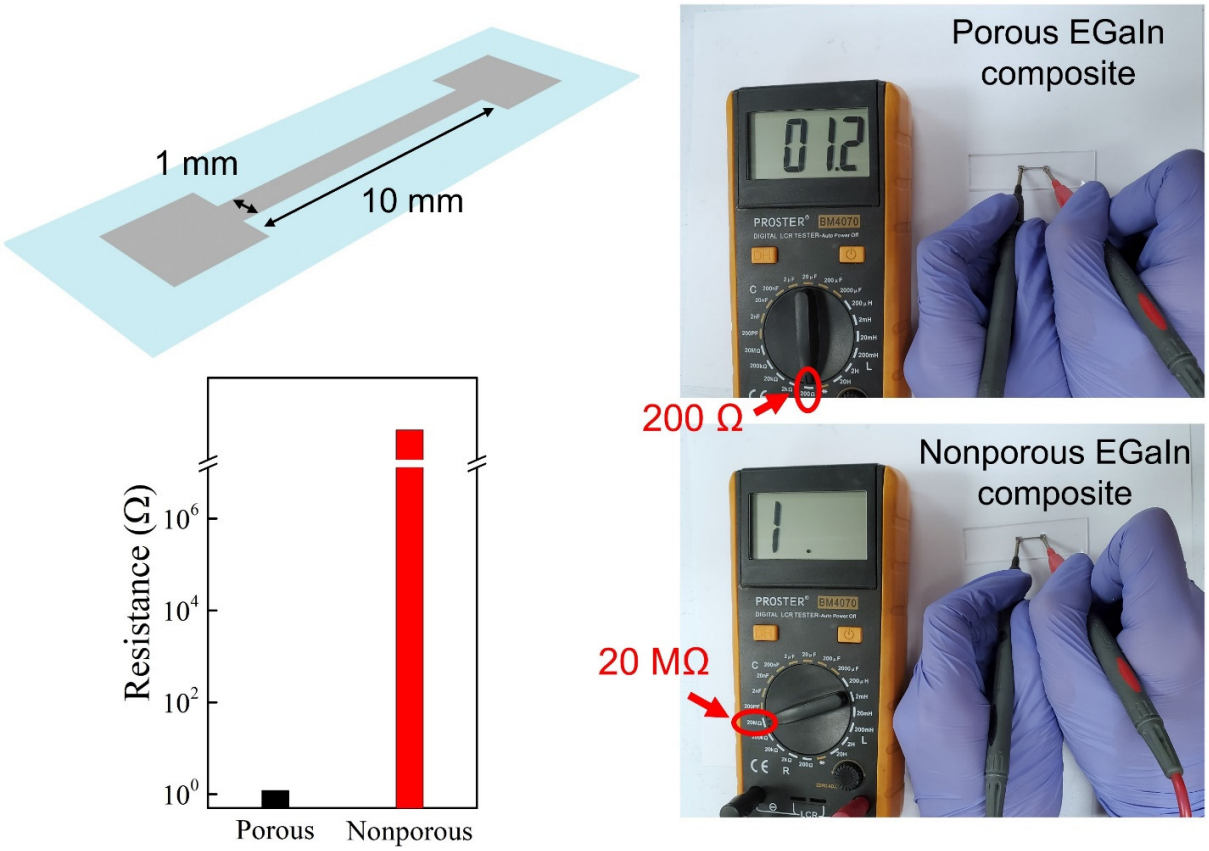

Figure S10. Comparisons of electrical resistances of nonporous and porous EGaIn composites with the same dimension and the same EGaIn fraction (~25% by volume). Here, the resistance of the porous EGaIn composite is ~1.2 Ω and the resistance of the nonporous EGaIn composite is undetectable. To reach the same electrical conductivity of porous composites (~ 25% EGaIn volume fraction), the EGaIn volume fraction in nonporous composites should be ~55% (Fig. 2b). Based on the percolation theory, $A = A_0 \times (V_f - V_c)^b$, where A and A_0 denote the electrical conductivities of the composite and bulk EGaIn, respectively, and V_f, V_c and b are the volume fraction of conductive fillers, percolation threshold, and fitting exponent, respectively (*10*). According to this theory, less amounts of EGaIn is needed in porous composites to reach the same electrical conductivity than that of nonporous EGaIn composites due to the dramatically reduced percolation threshold (Fig. 2A). The dramatically reduced percolation threshold mainly arises from the non-uniform distribution of EGaIn particles in porous composites, which self-organize on the pore surfaces during phase separation (fig. S3).

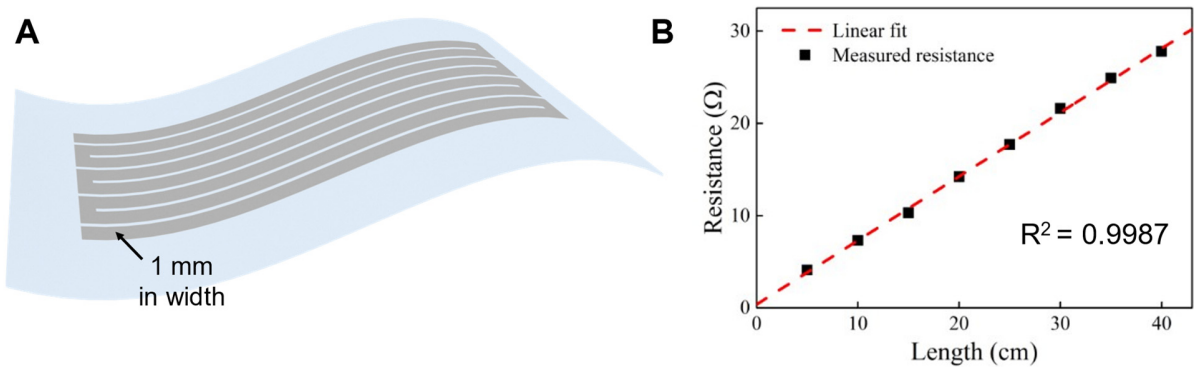

Figure S11. Electrical uniformity of porous EGaIn composites. Schematic illustration (**A**) and electrical resistances as a function of the length of the conductive trace (**B**), showing high electrical uniformity of phase-separation-synthesized porous EGaIn-PU composites over a large area.

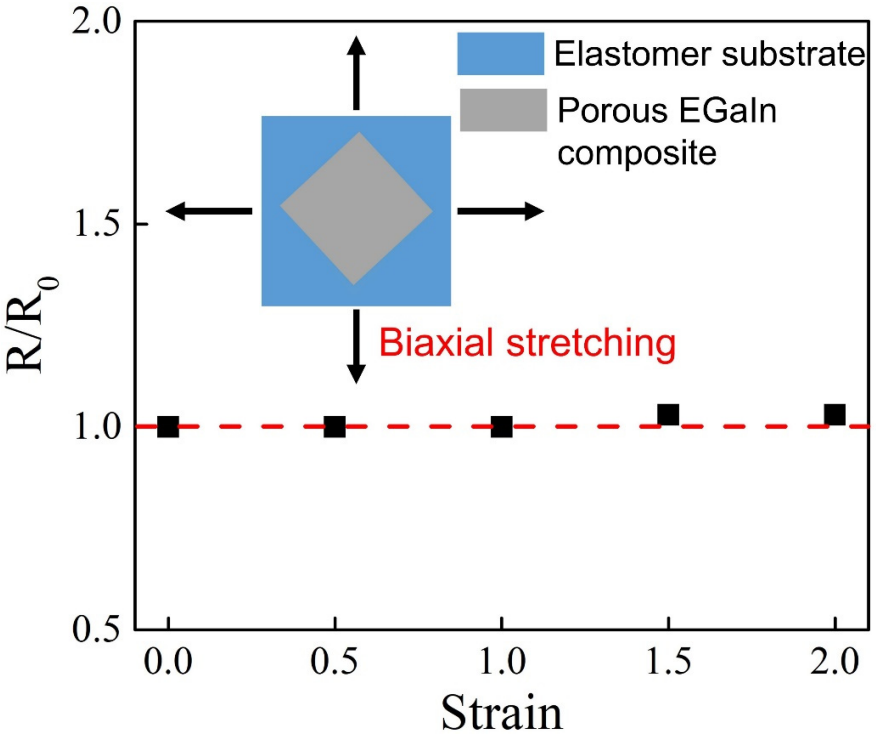

Figure S12. Relative resistance changes (R/R_0) of porous EGaIn composites as a function of equally biaxial strains, indicating outstanding mechanical-electrical decoupling. In particular, the resistance changes ~3% at 200% biaxal strain.

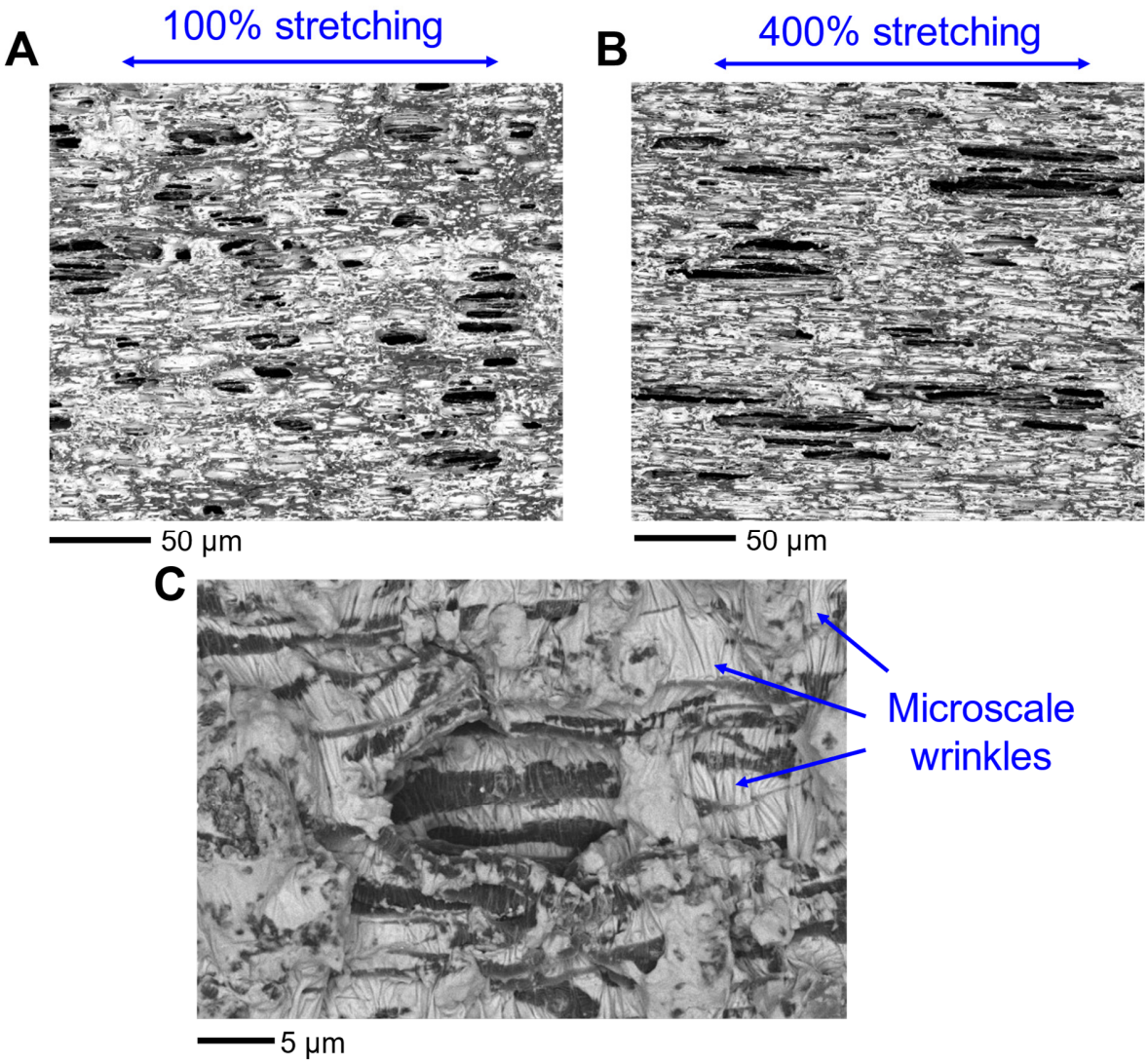

Figure S13. SEM characterizations of porous EGaIn composites. SEM images of porous EGaIn composites under 100% (**A**) and 400% (**B**) uniaxial stretching, indicating the fluid-like property of liquid metal and reorientation of conductive paths along the stretching direction. **C**, High-resolution SEM image of porous EGaIn composites, demonstrating microscale wrinkles formed on EGaIn conductive pathways. As compared to the results in fig. S3, the porous EGaIn composites in fig. S13 were activated by mechanical sintering (i.e., collapsing EGaIn particles into conductive pathways).

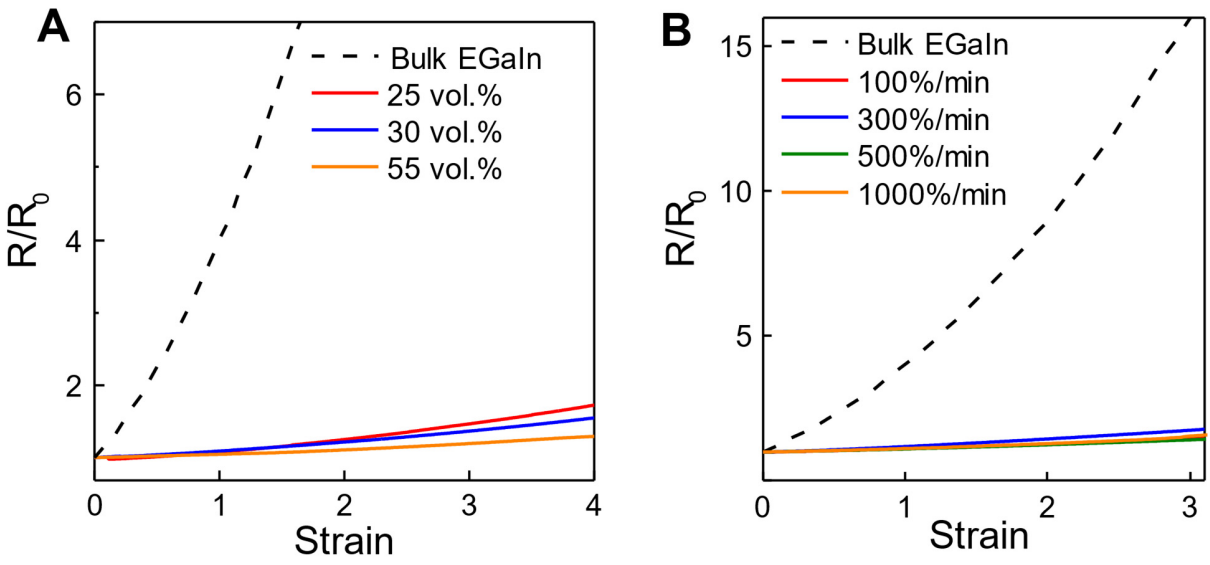

Figure S14. Effects of EGaIn contents and stretching rates on electrochemical responses of porous EGaIn composites. Experiments indicate that the EGaIn volume fraction (**A**) and the stretching rate (**B**) have small effects on the electrochemical responses of porous EGaIn composites, indicating promising electrical-mechanical decoupling.

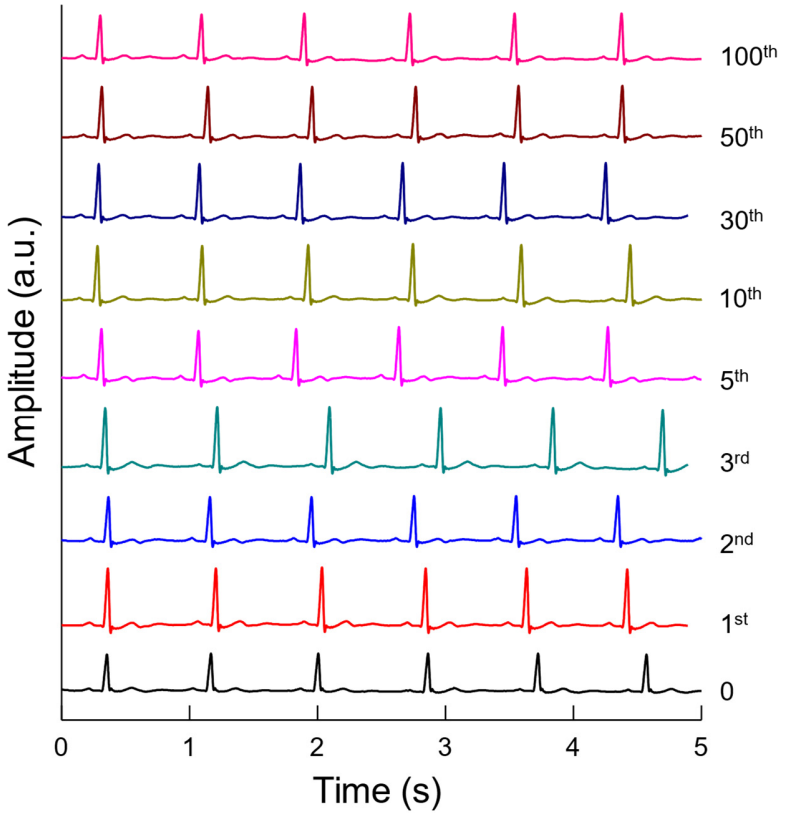

Figure. S15. ECG signals recorded with porous EGaIn composites after various repetitive peeling cycles using scotch tapes. The results showed negligible signal degradation after up to 100 peeling cycles.

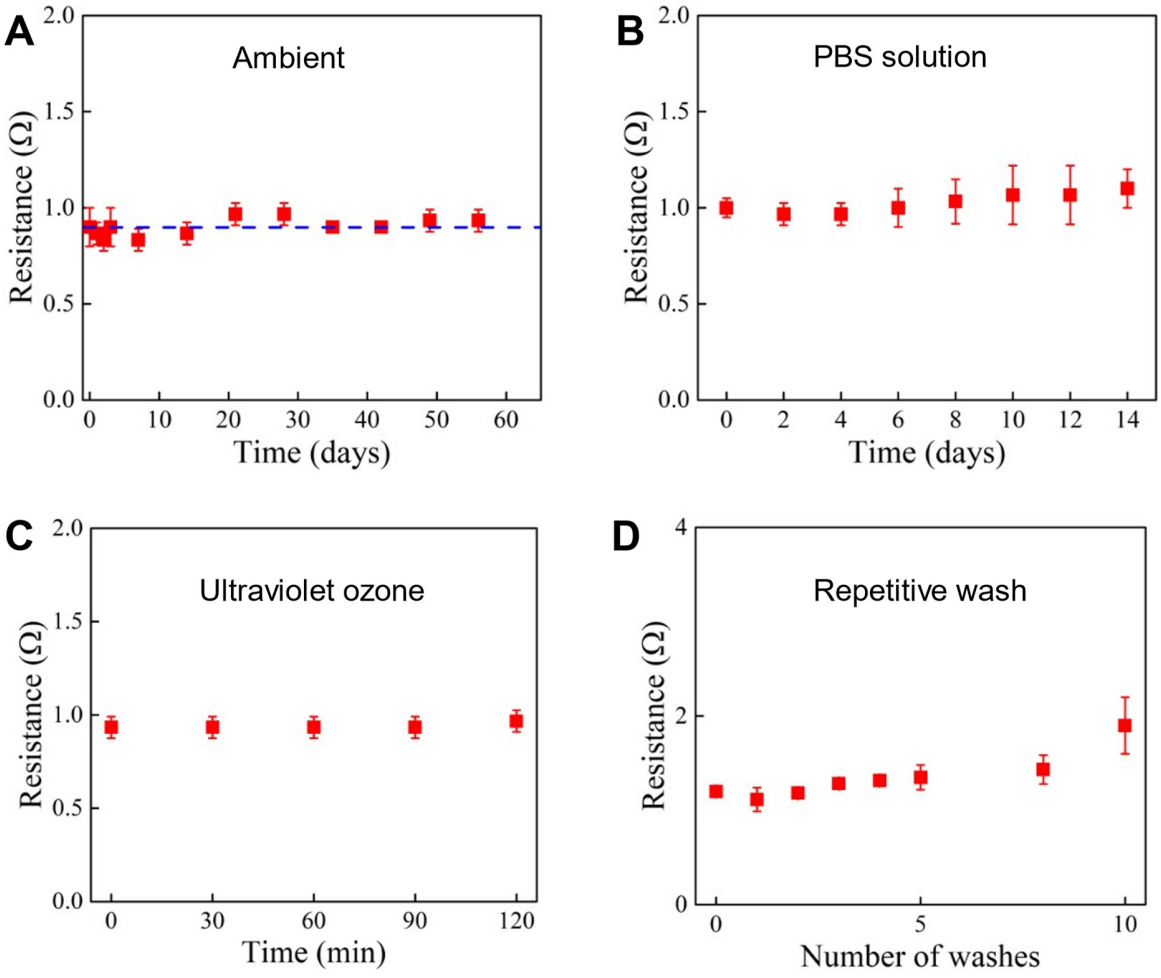

Figure S16. Stability tests of porous EGaIn composites under various conditions. Resistance variations of porous EGaIn composites as a function of the elapsed time under ambient conditions (**A**), in PBS solutions (**B**), and by ultraviolet ozone treatment (**C**), and after repetitive washing (**D**) showing high electrical stability.

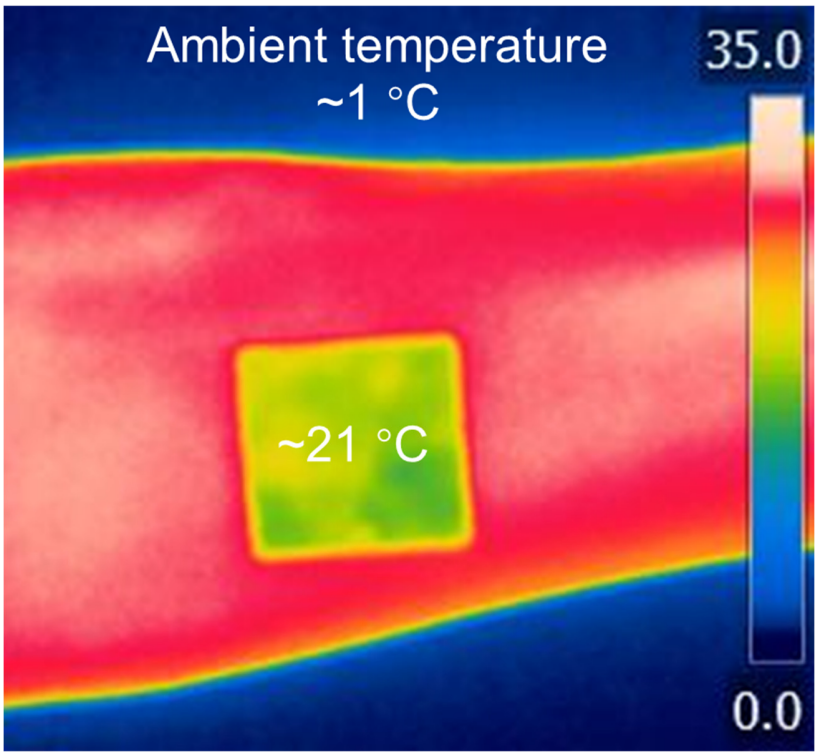

Figure S17. Thermal mapping images of the porous EGaIn composite on the human forearm. The porous composite temperature (~21 °C) is much higher than the ambient temperature (~1 °C) and would be substantially higher than its freezing temperature. Given the supercooling effect *(27)* and skin-interfaced applications, the porous composite is capable of working in low-temperature scenarios.

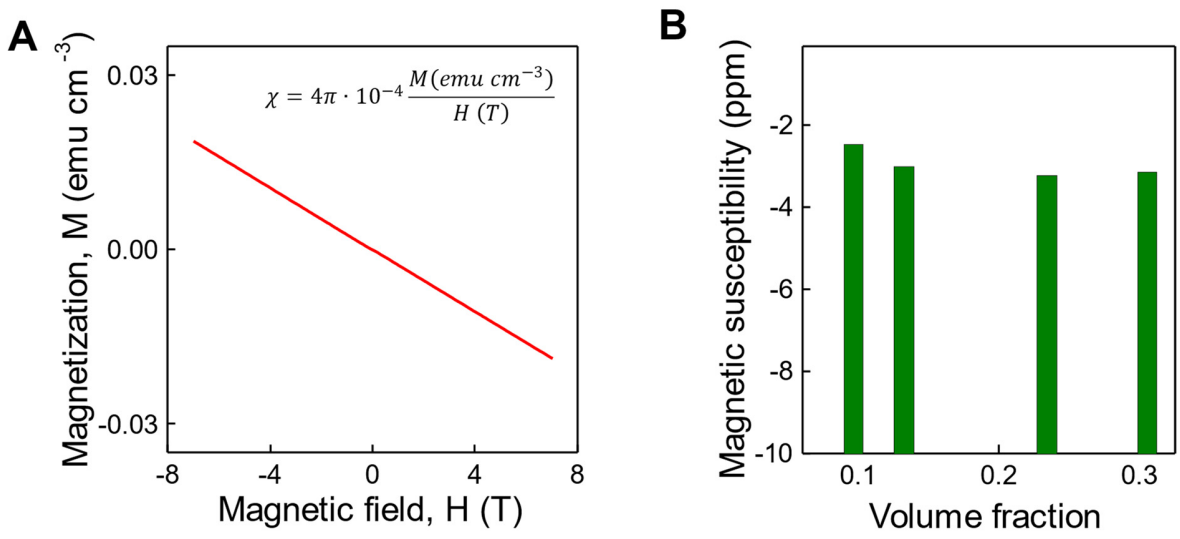

Figure S18. Magnetization of porous EGaIn composite measured at 300 K for applied magnetic fields up to 7T. The magnetic susceptibility (χ) of porous EGaIn composite determined by the inset equation is -3.23 ppm (**A**), and negligibly depends on the volume fractions (**B**).

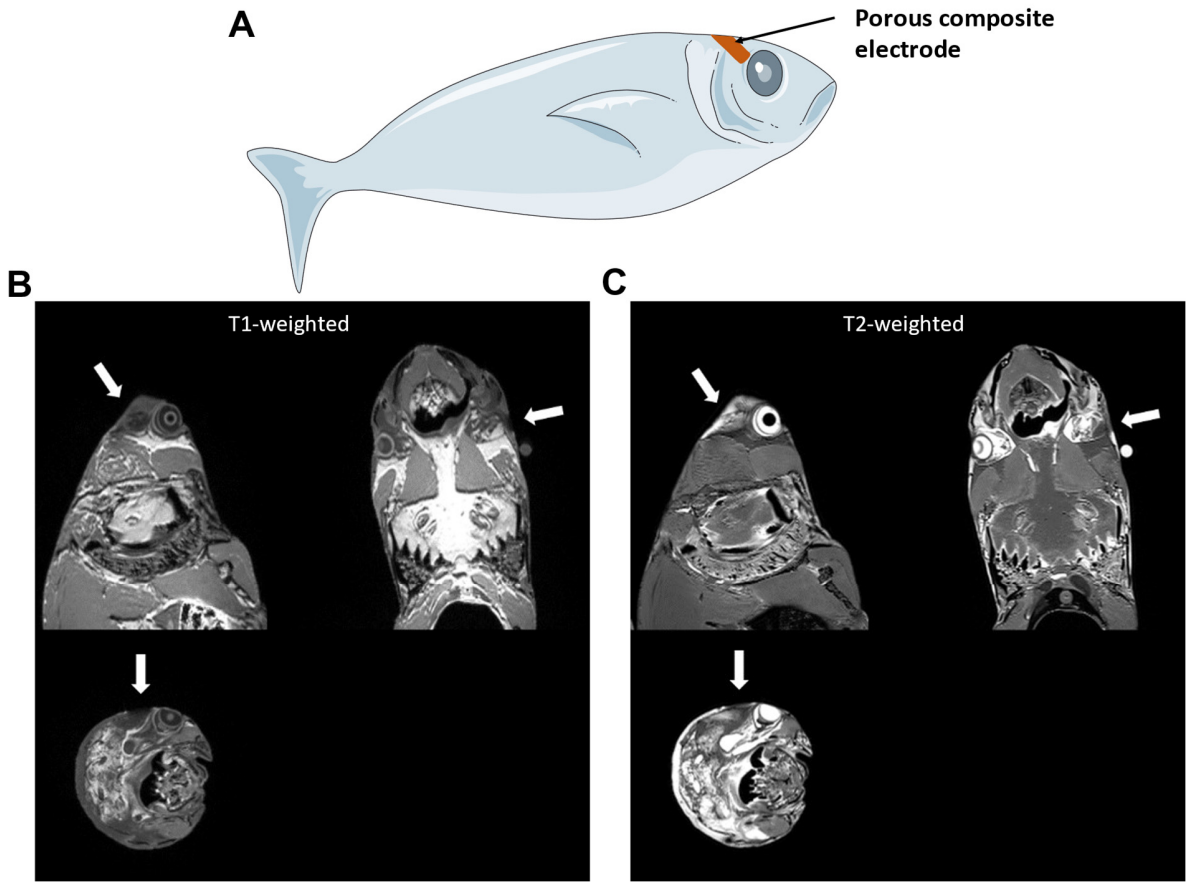

Figure S19. MRI compatibility of porous EGaIn composites. A, Schematic illustration of the location of porous EGaIn composite on a fish head. **B,** T1-weighted magnetization prepared rapid acquisition gradient echo (MPRAGE) sequence scans. **C,** T2-weighted sampling perfection with application optimized contrasts using different flip angle evolution (SPACE) sequence scans. The arrows indicate the location of porous EGaIn composites on the fish head.

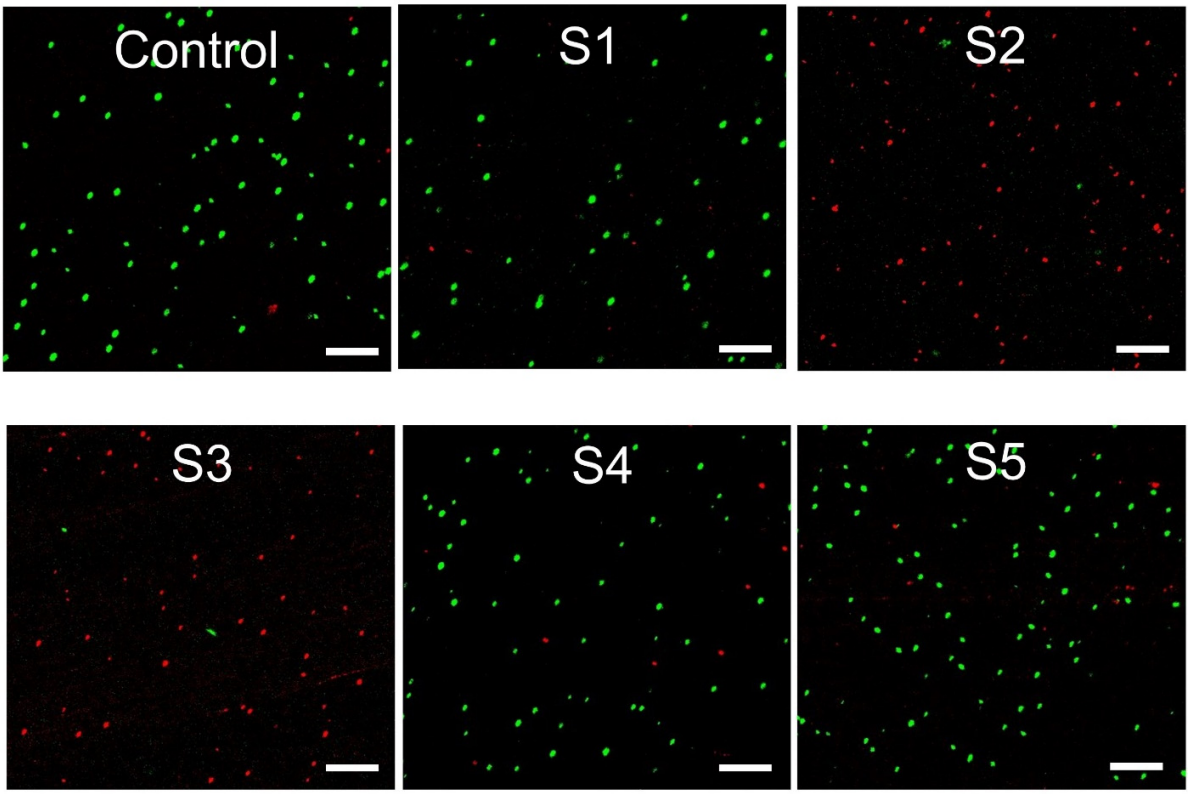

Figure S20. Fluorescent live/dead staining images of MRSA conditioned with various materials for two hours. Green and red represent live and dead MRSA bacterial cells, respectively. Control: tissue culture polystyrene; S1: porous EGaIn composite without ε-PL; S2: porous EGaIn composite with ε-PL; S3: porous PU with ε-PL; S4: porous PU without ε-PL; S5: AgNWs-PU composite. Scale bars: 50 μm.

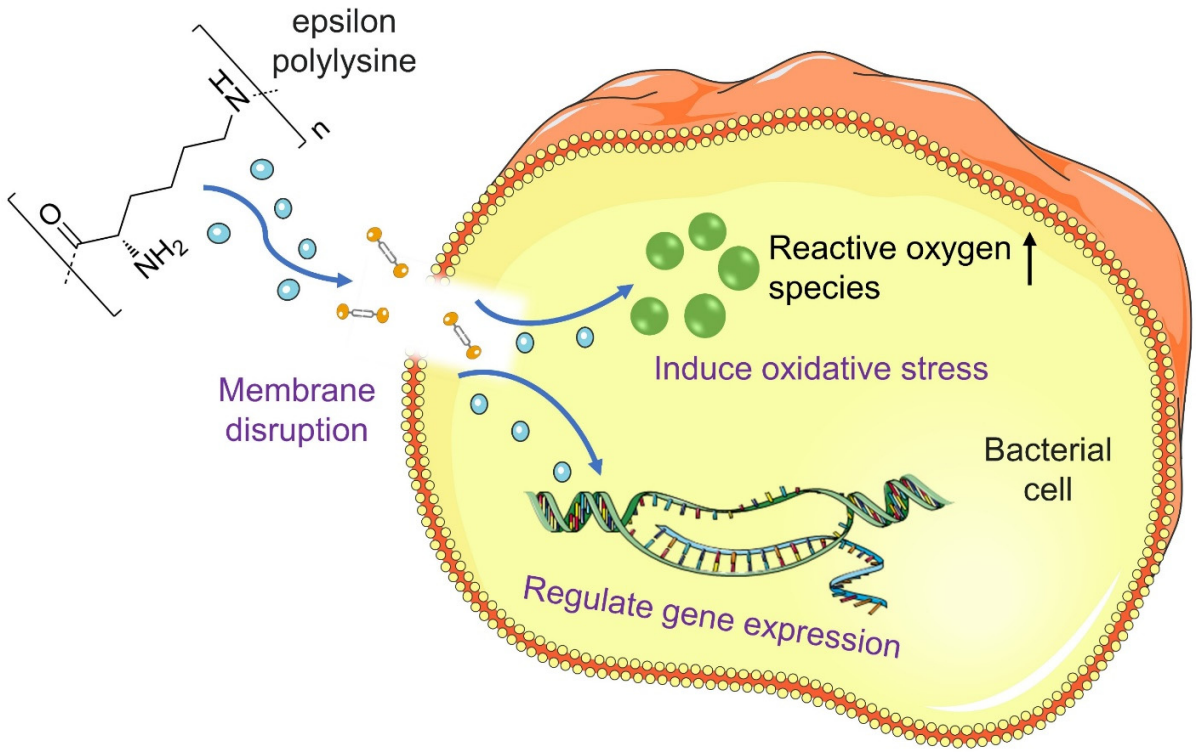

Figure S21. Schematic illustration of the antibacterial mechanism of epsilon polylysine. Positively charged epsilon polylysine is readily targeted to negatively charged bacterial cell membrane due to the electrostatic attraction. The accumulation of attached epsilon polylysine cations can cause membrane disruption and therefore invade into the cytoplasm. Accordingly, this can induce generation of reactive oxygen species and DNA damage response, regulate related gene expression, and finally leads to bacterial cell death (*21*).

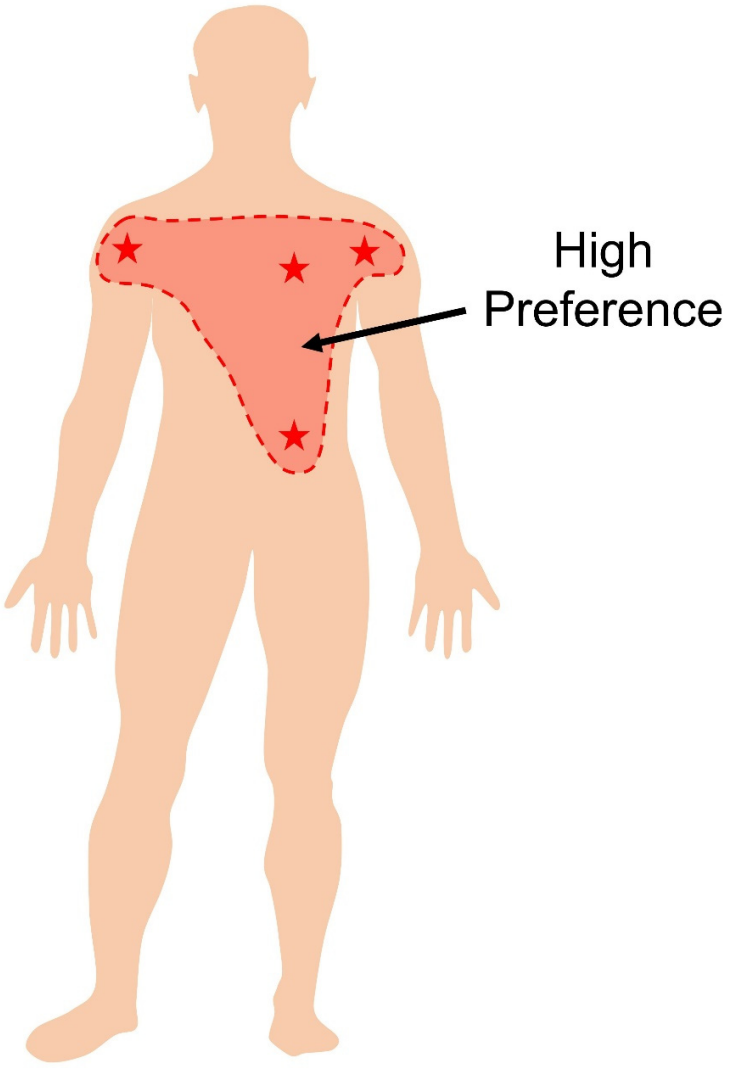

Figure S22. Schematic of the user-preference locations for placing wearable bioelectronics. The highlighted area with red asterisks indicates highly preferred body locations for wearable device placement (*52*). Thus, in this research, on-skin patches (1 × 1 cm^2) made of various soft materials were laminated on human chest skins for five days to examinate their effects on skin bacterial symbiosis.

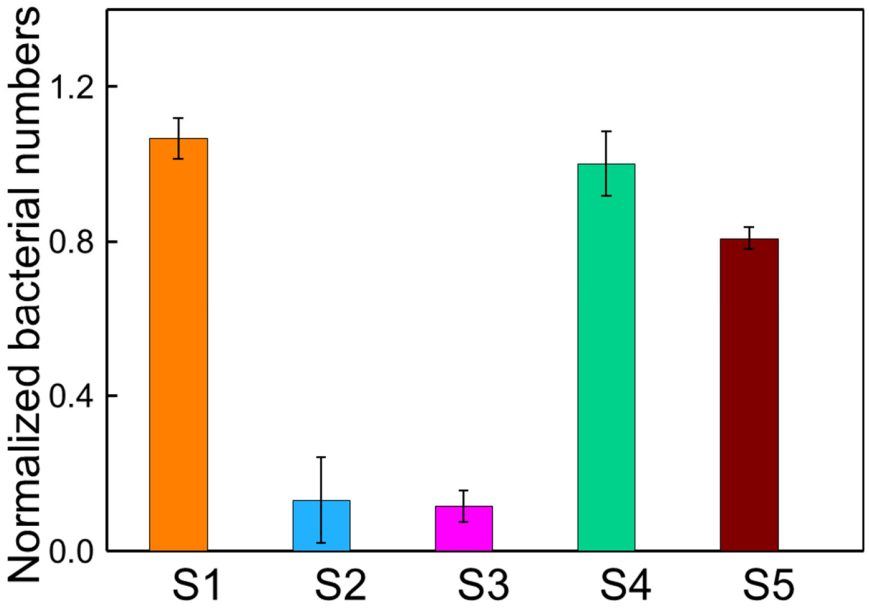

Figure S23. Normalized bacterial numbers on skin patches after five-day on-body wearing. S1, porous composite w/o ε-PL; S2, porous composite w/ ε-PL; S3, porous PU w/ ε-PL; S4, porous PU w/o ε-PL; S5, AgNWs composite.

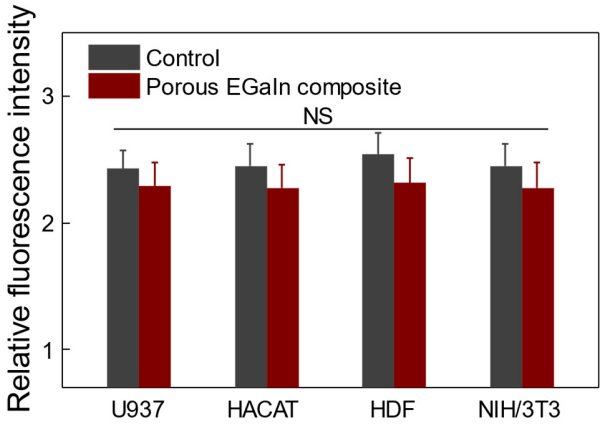

Figure S24. In vitro biocompatibility evaluations in sweaty conditions. Relative fluorescence intensities of the control sample and the porous EGaIn composite with ε-PL after 1,000 cycles of 50% repetitive stretching in artificial perspiration (pH 4.3) after five-day incubations of U937, HaCaT, HDF, and NIH/3T3 cell lines.

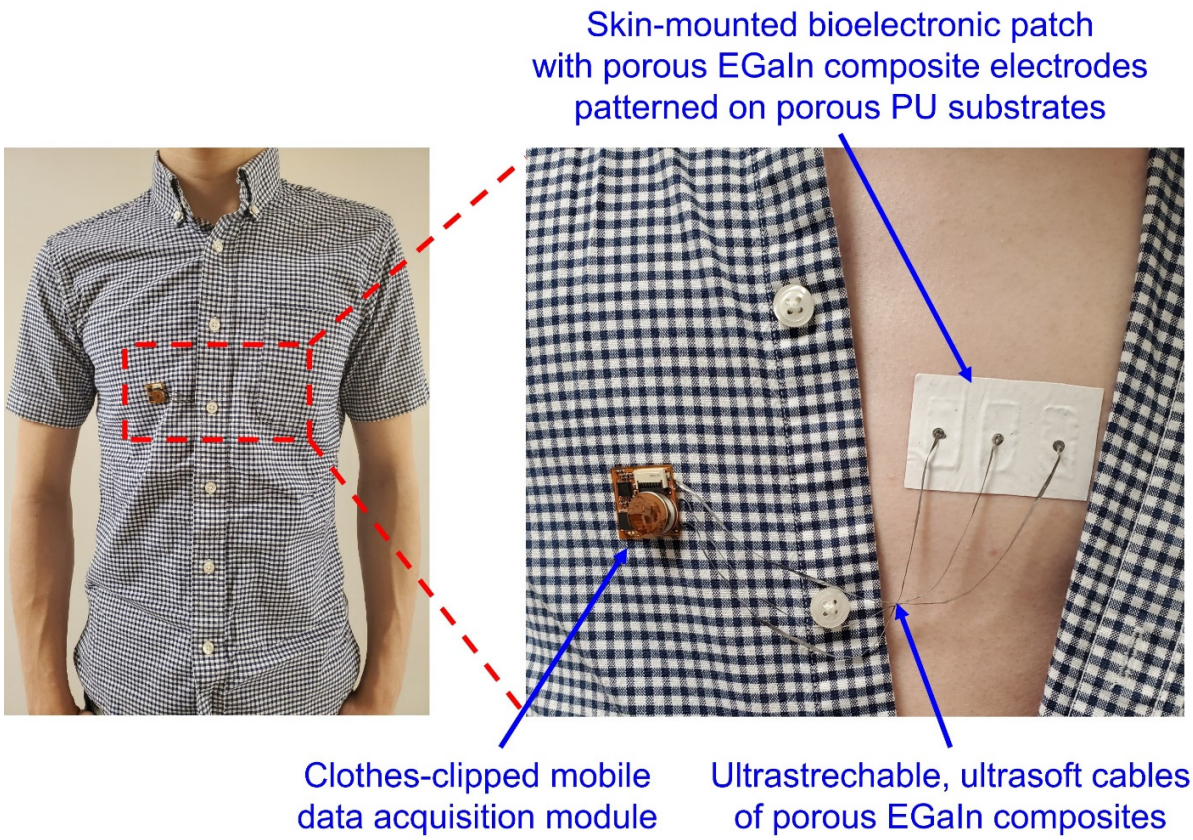

Figure S25. Photographs of the skin-interfaced bioelectronic system based on porous EGaIn composites. The wearable system comprises the skin-mounted bioelectronic patch with porous EGaIn composite electrodes patterned on porous PU supporting substrates and mobile data acquisition module clipped onto clothing. Conductive cables of porous EGaIn composites are used to interconnect the skin-mounted bioelectronic patch with the mobile data acquisition module. Here, both skin-mounted bioelectronic patches and interconnect cables are fabricated by solution process, which are low-cost, disposable, and one-time use to further minimize infection risks. Mobile data acquisition modules are assembled with off-the-shelf electronic components and reusable to save cost. The whole wearable system is mechanically imperceptible to users, interact with human body in a long-term biocompatible and comfortable manner, and can perform high-fidelity biosignal recording even during human motions because both the skin-interfaced devices and cables are made of porous electronic materials that can simultaneously achieve outstanding leakage resistance, antimicrobial property, large stretchability, ultrasoftness, high and invariable electrical conductivity over strains, and high breathability. The MRI compatibility can benefit the applications where physiological monitoring is needed to provide complementary information to MRI imaging.

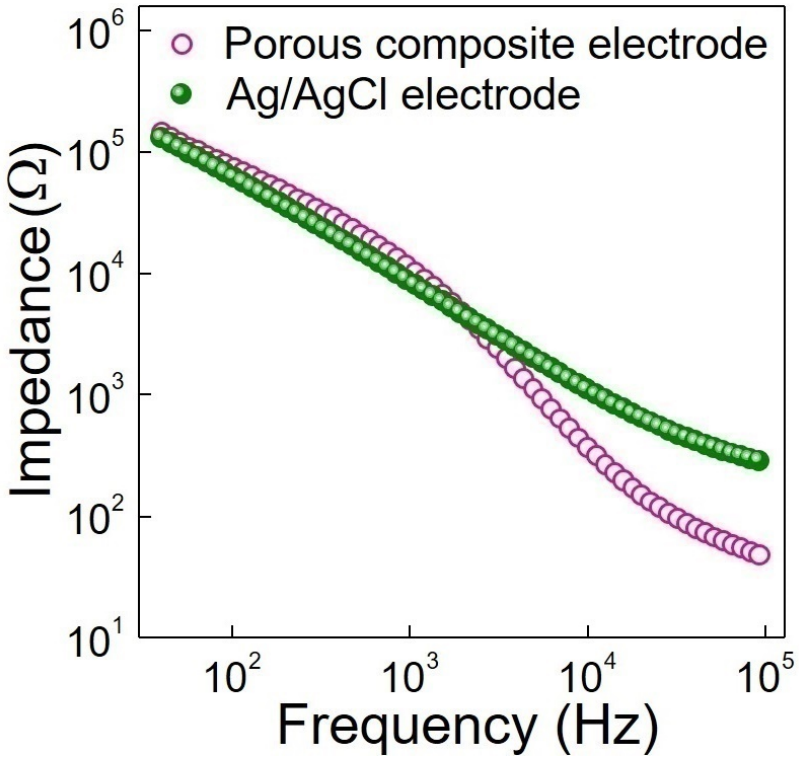

Figure S26. Skin-electrode impedances of porous EGaIn composite electrodes and conventional Ag/AgCl gel electrodes.

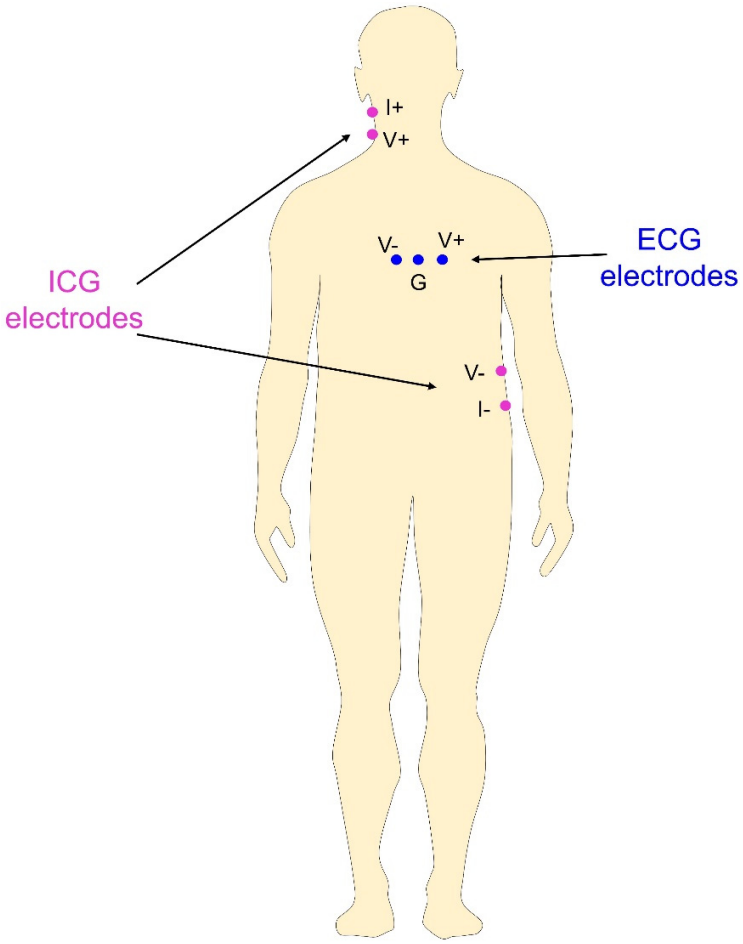

Figure S27. Schematic illustrations of ICG and ECG electrodes placements on human body. The ICG signal was captured by a classic tetrapolar array, where the positive current electrode (I+) was placed on neck and the negative current electrode (I-) was placed near the thorax 3 cm below the xiphisterna junction. The other two inner voltage electrodes (V+, V-) were 3 cm away from each current electrode. The ECG electrodes, comprising positive (V+), negative (V-) and ground (G) electrodes, were placed on chest.

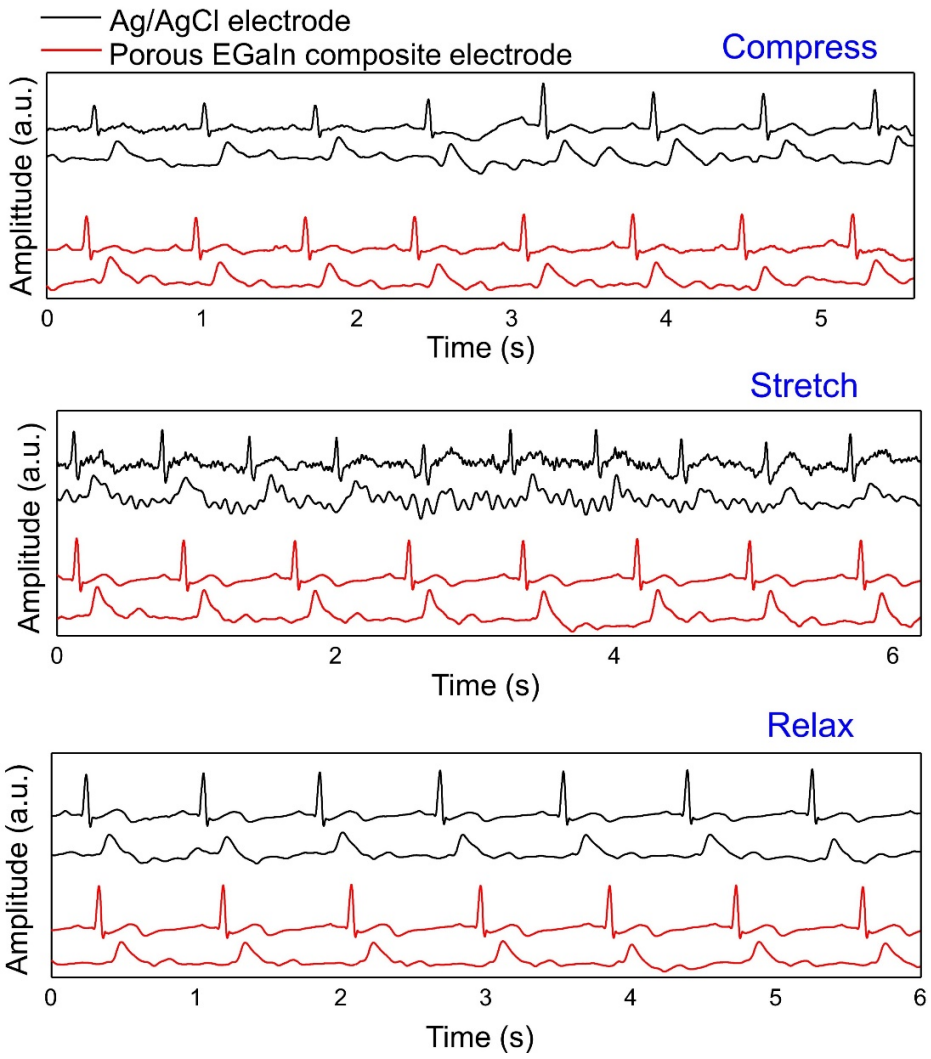

Figure S28. ECG and ICG signals recorded by Ag/AgCl electrodes (black) and porous EGaIn composite electrodes (red) when compressing, stretching, and relaxing these electrodes. The results indicate that porous EGaIn composite electrodes can operate stably and reliably under various mechanical deformations due to their ultrasoftness and ultrastretchability (retaining conformal contacts with skin during dynamic deformation) and negligible conductance change over strain (minimizing conductance-change induced noises). By contrast, notable motion artifacts are observed in biosignals recorded by conventional Ag/AgCl electrodes.

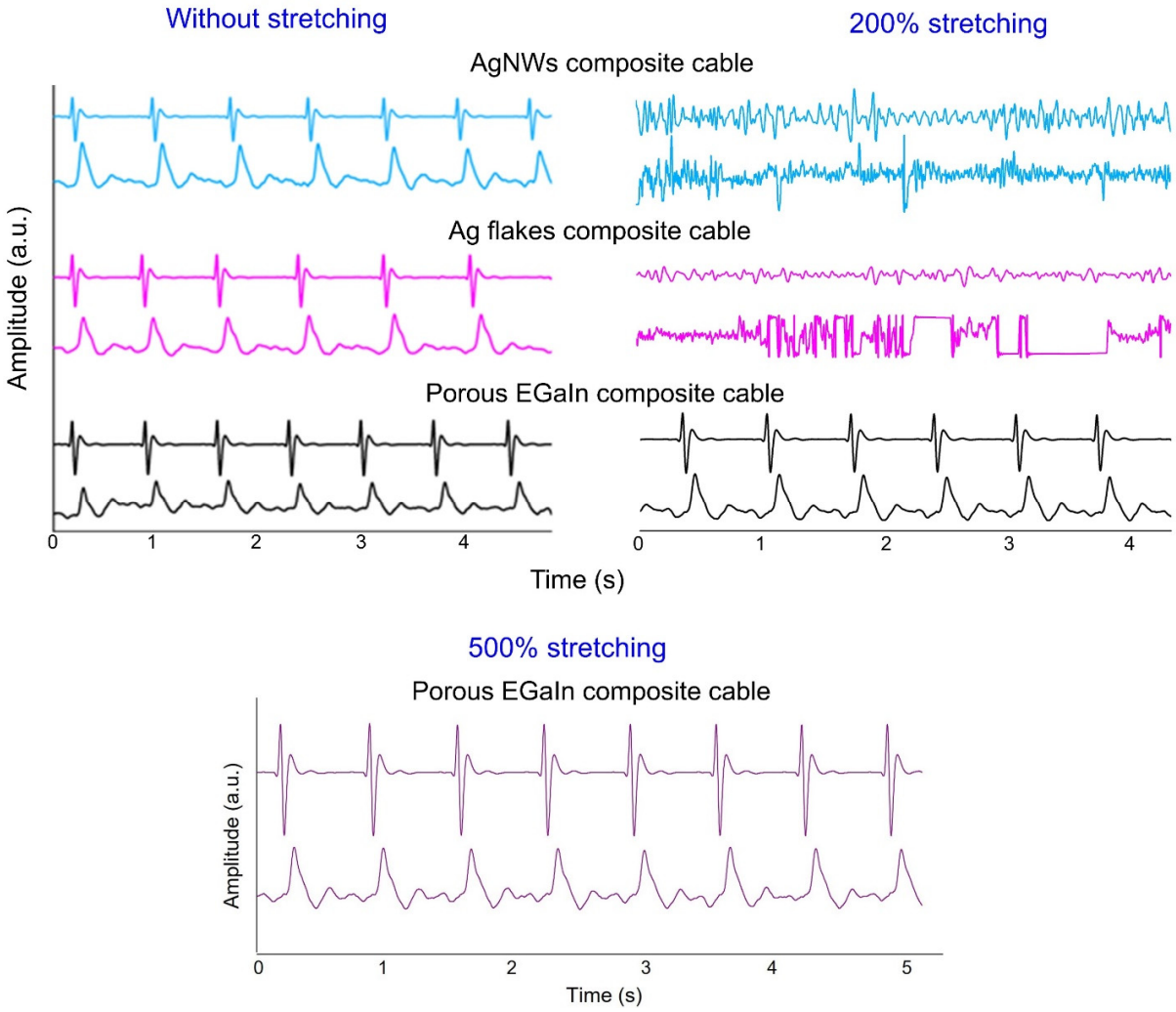

Figure S29. ECG and ICG signals recorded using porous EGaIn composite electrodes when stretching various cables with 0%, 200% and 500% strains. As compared to interconnection cables made of other composite materials, the results indicate that the porous EGaIn composite cable can operate stably and reliably under large strains due to its ultrastretchability and negligible conductance change with strain. Here, the AgNWs composite cable and Ag flakes composite cable were broken and not conductive at 500% stretching.

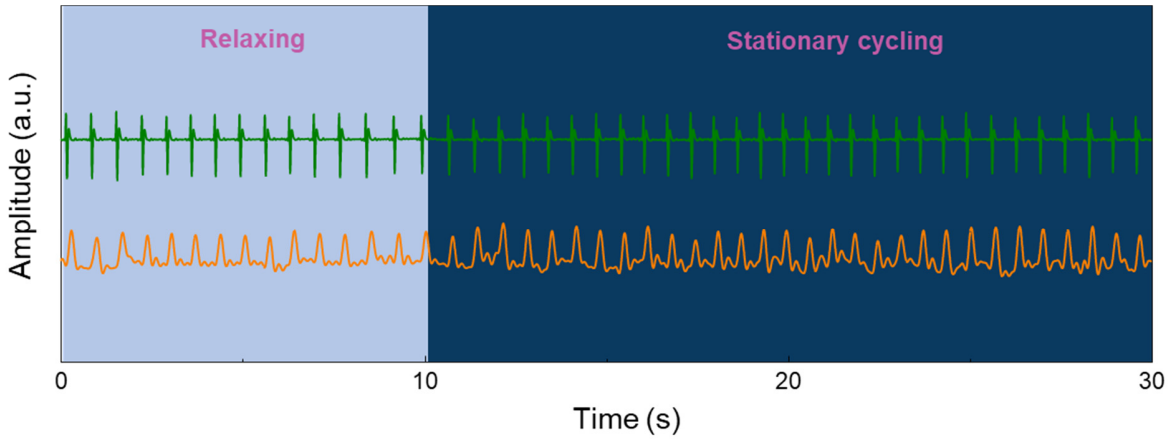

Figure S30. Simultaneous monitoring of ECG and ICG using skin-interfaced bioelectronics based on porous EGaIn composites when a human subject was cycling on a stationary bicycle.

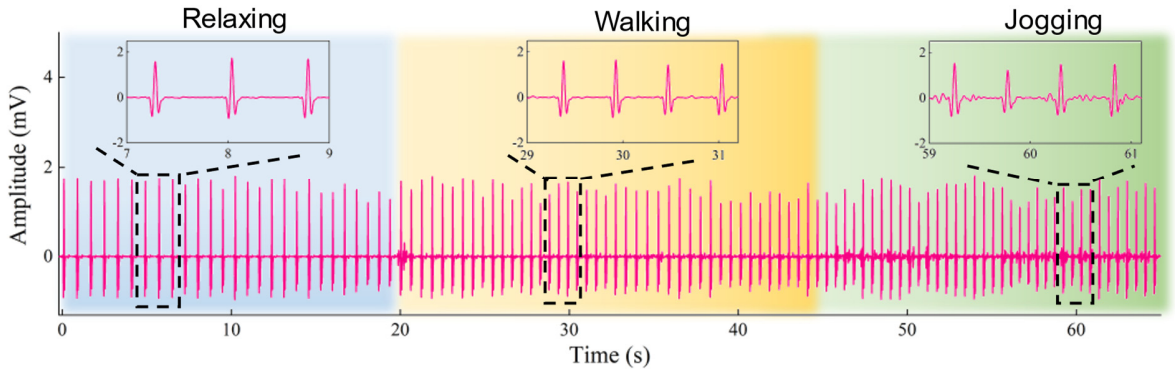

Figure S31. ECG signals recorded using the wearable system, shown in fig. S25, when human subject relaxed (blue), walked (orange) and jogged (green) on a treadmill. The signal-to-noise ratios during relaxing, walking and jogging are 41 dB, 37 dB and 34 dB, respectively. The results indicate that the wearable system based on porous EGaIn composites can perform high-fidelity signals during human motions.

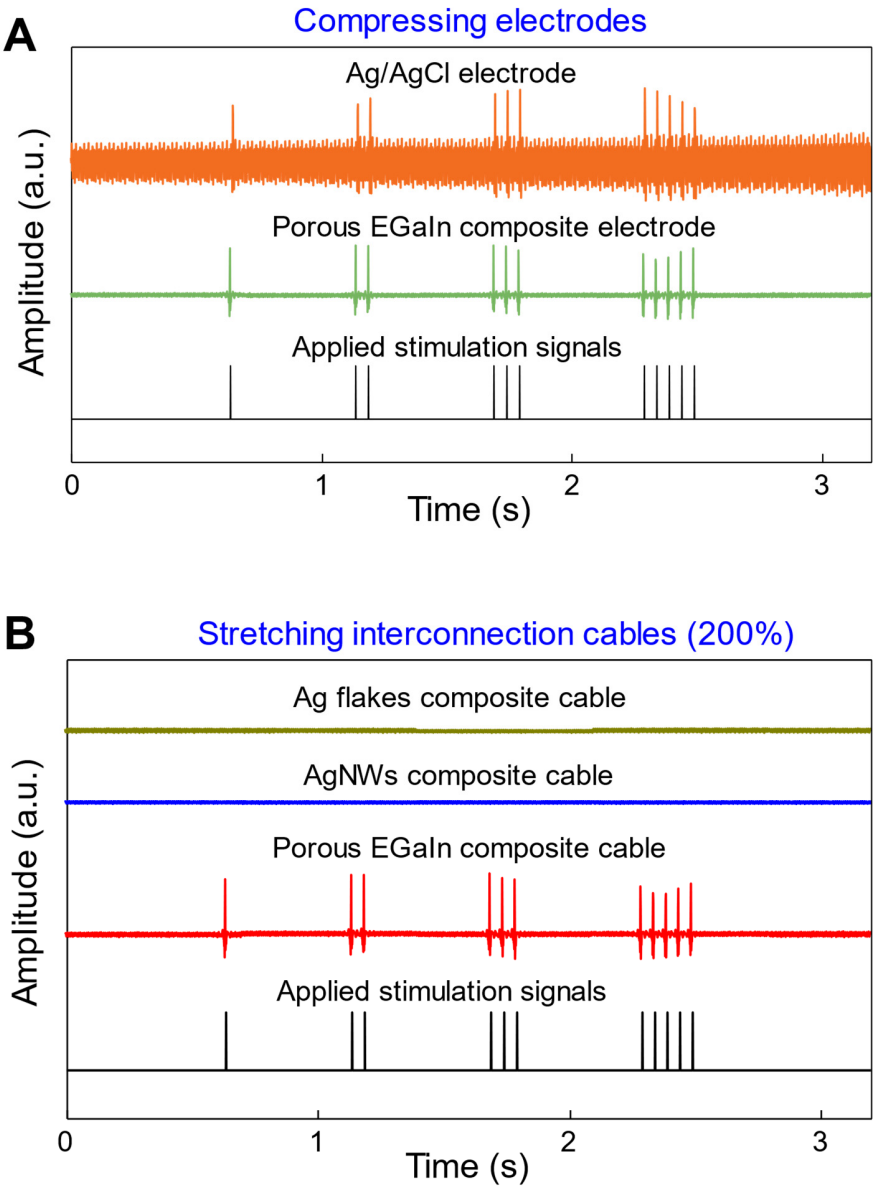

Figure S32. Programmed on-skin electrical stimulations during deformations. A, Applied electrical stimulation signals (black) and induced EMG signals when compressing porous EGaIn composite (green) and conventional Ag/AgCl (orange) stimulation electrodes. **B**, Applied electrical stimulation signals (black) and induced EMG signals when interconnection cables of porous EGaIn composite (red), AgNWs composite (blue) and Ag flakes composite (green) were stretched (200% strain). Muscle contractions were not successfully stimulated when stretching the interconnection cables of AgNWs composite and Ag flakes composite with a large strain (200%). The results indicate that wearable devices based porous EGaIn composites can apply stable and programmed electrical stimulations on human bodies even under mechanical deformations.

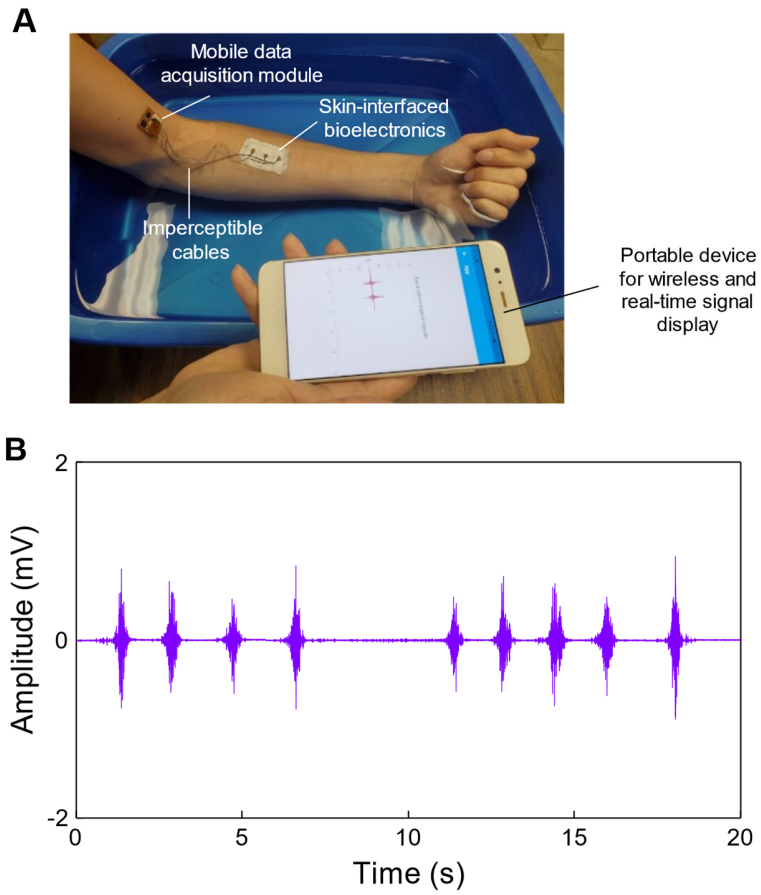

Figure S33. EMG recording in water. A, A photograph of EMGs signal recording in water. **B**, The EMG signals recorded in water, showing the uncompromised signal quality.

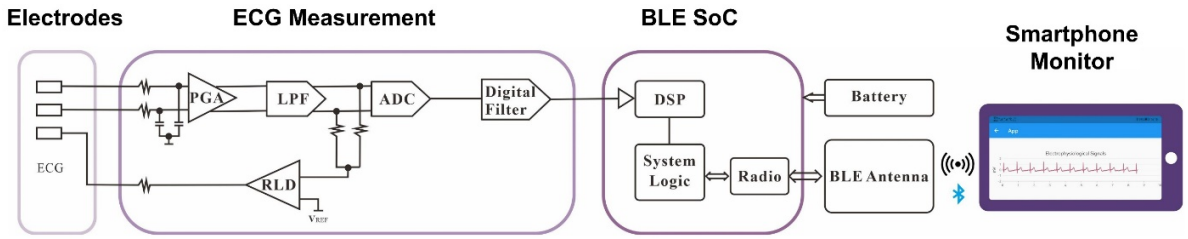

Figure S34. The detailed block diagram of the mobile data acquisition circuit. LPF: low-pass filter; ADC: analog-to-digital converter; PGA: programmable gain amplifier; DSP: digital signal processor; RLD: right leg driver; BLE: Bluetooth Low Energy; and SoC: system on a chip.

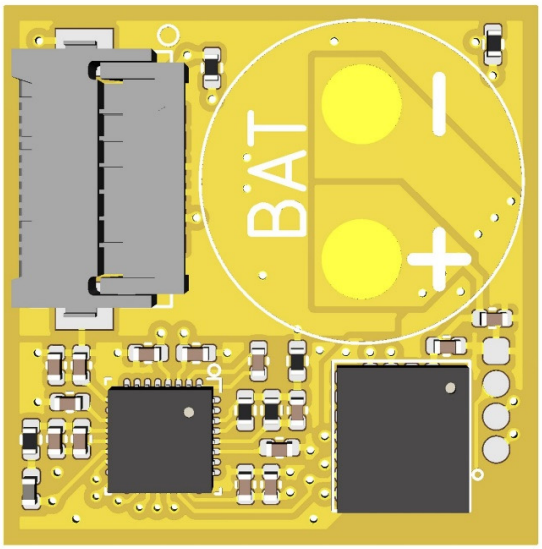

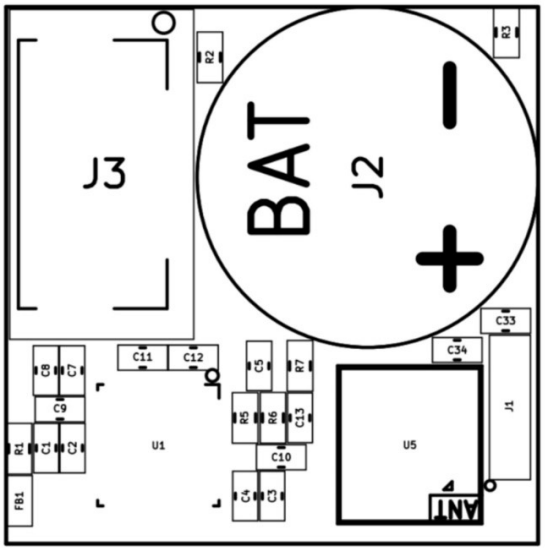

Components	Value	Description
C1, C3, C8, C33	10uF	Power filter capacitor
C2, C4, C7, C34	0.1uF	Power filter capacitor
C5	10nF	Signal filter capacitor
C9, C10	1uF	Signal filter capacitor
C11, C12, C13	1.5nF	Signal filter capacitor
FB1	Ferrite bead	Power line filter
R1	2.2ohm	Power line filter
R2, R3	51.1Kohm	Filter resistor
R5, R7	100Kohm	Protection resistor
R6	1Mohm	Feedback resistor
U1	ADS1291	Electrophysiology front end IC
U5	HJ-185MH	Bluetooth and controller IC
J3	6Pin connector	FPC connector

Figure S35. Schematic and list of off-the-shelf electronic components used in the mobile data acquisition module.

Material	Young's modulus	Poisson's ratio
Porous composite	1.5 MPa	0.2
PU	15 MPa	0.4
ACF cable	3 GPa	0.34
EGaIn	Bulk modulus 50 MPa (*53*) Shear modulus 1 kPa (*53*)	Not used
Epidermis	2.5 MPa (*54*)	0.4
Dermis	10 MPa (*55*)	0.4

Table S1. Material properties used for FEA simulations.

Movie S1 Wireless ECG recordings with dynamic human motions

Movie S2 Waterproof wireless EMG recordings

REFERENCES AND NOTES

1. J. A. Rogers, T. Someya, Y. Huang, Materials and mechanics for stretchable electronics. *Science* **327**, 1603–1607 (2010).

2. D. H. Kim, N. Lu, R. Ma, Y. S. Kim, R. H. Kim, S. Wang, J. Wu, S. M. Won, H. Tao, A. Islam, K. J. Yu, T. I. Kim, R. Chowdhury, M. Ying, L. Xu, M. Li, H. J. Chung, H. Keum, M. McCormick, P. Liu, Y. W. Zhang, F. G. Omenetto, Y. Huang, T. Coleman, J. A. Rogers, Epidermal electronics. *Science* **333**, 838–843 (2011).

3. D. C. Kim, H. J. Shim, W. Lee, J. H. Koo, D. H. Kim, Material-based approaches for the fabrication of stretchable electronics. *Adv. Mater.* **32**, 1902743 (2020).

4. K. Sim, Z. Rao, F. Ershad, C. Yu, Rubbery electronics fully made of stretchable elastomeric electronic materials. *Adv. Mater.* **32**, 1902417 (2020).

5. T. C. Shyu, P. F. Damasceno, P. M. Dodd, A. Lamoureux, L. Xu, M. Shlian, M. Shtein, S. C. Glotzer, N. A. Kotov, A kirigami approach to engineering elasticity in nanocomposites through patterned defects. *Nat. Mater.* **14**, 785–789 (2015).

6. T. Someya, Z. Bao, G. G. Malliaras, The rise of plastic bioelectronics. *Nature* **540**, 379–385 (2016).

7. Y. Ohm, C. Pan, M. J. Ford, X. Huang, J. Liao, C. Majidi, An electrically conductive silver–polyacrylamide–alginate hydrogel composite for soft electronics. *Nat. Electron.* **4**, 185–192 (2021).

8. K. Sakuma, *Flexible, Wearable, and Stretchable Electronics* (CRC Press, 2020).

9. S. Choi, S. I. Han, D. Jung, H. J. Hwang, C. Lim, S. Bae, O. K. Park, C. M. Tschabrunn, M. Lee, S. Y. Bae, J. W. Yu, J. H. Ryu, S. W. Lee, K. Park, P. M. Kang, W. B. Lee, R. Nezafat, T. Hyeon, D. H. Kim, Highly conductive, stretchable and biocompatible Ag-Au core-sheath nanowire composite for wearable and implantable bioelectronics. *Nat. Nanotechnol.* **13**, 1048–1056 (2018).

10. Y. Kim, J. Zhu, B. Yeom, M. di Prima, X. Su, J. G. Kim, S. J. Yoo, C. Uher, N. A. Kotov, Stretchable nanoparticle conductors with self-organized conductive pathways. *Nature* **500**, 59–63 (2013).

11. N. Matsuhisa, D. Inoue, P. Zalar, H. Jin, Y. Matsuba, A. Itoh, T. Yokota, D. Hashizume, T. Someya, Printable elastic conductors by in situ formation of silver nanoparticles from silver flakes. *Nat. Mater.* **16**, 834–840 (2017).

12. S. Chen, H.-Z. Wang, R.-Q. Zhao, W. Rao, J. Liu, Liquid metal composites. *Matter* **2**, 1446–1480 (2020).

13. E. J. Markvicka, M. D. Bartlett, X. Huang, C. Majidi, An autonomously electrically self-healing liquid metal–elastomer composite for robust soft-matter robotics and electronics. *Nat. Mater.* **17**, 618–624 (2018).

14. Y. Liu, X. Ji, J. Liang, Rupture stress of liquid metal nanoparticles and their applications in stretchable conductors and dielectrics. *npj Flex. Electron.* **5**, 11 (2021).

15. L. Zheng, M. Zhu, B. Wu, Z. Li, S. Sun, P. Wu, Conductance-stable liquid metal sheath-core microfibers for stretchy smart fabrics and self-powered sensing. *Sci. Adv.* **7**, eabg4041 (2021).

16. Z. Ma, Q. Huang, Q. Xu, Q. Zhuang, X. Zhao, Y. Yang, H. Qiu, Z. Yang, C. Wang, Y. Chai, Z. Zheng, Permeable superelastic liquid-metal fibre mat enables biocompatible and monolithic stretchable electronics. *Nat. Mater.* **20**, 859–868 (2021).

17. S. Xu, A. Jayaraman, J. A. Rogers, Skin sensors are the future of health care. *Nature* **571**, 319–321 (2019).

18. C. Marambio-Jones, E. Hoek, A review of the antibacterial effects of silver nanomaterials and potential implications for human health and the environment. *J. Nanopart. Res.* **12**, 1531–1551 (2010).

19. A. K. Chatterjee, R. Chakraborty, T. Basu, Mechanism of antibacterial activity of copper nanoparticles. *Nanotechnology* **25**, 135101 (2014).

20. J. J. Kim, S. Ha, L. Kim, Y. Kato, Y. Wang, C. Okutani, H. Wang, C. Wang, K. Fukuda, S. Lee, T. Yokota, O. S. Kwon, T. Someya, Antimicrobial second skin using copper nanomesh. *Proc. Natl. Acad. Sci. U.S.A.* **119**, e2200830119 (2022).

21. R. Ye, H. Xu, C. Wan, S. Peng, L. Wang, H. Xu, Z. P. Aguilar, Y. Xiong, Z. Zeng, H. Wei, Antibacterial activity and mechanism of action of ε-poly-l-lysine. *Biochem. Biophys. Res. Commun.* **439**, 148–153 (2013).

22. Y.-Q. Li, Q. Han, J.-L. Feng, W.-L. Tian, H.-Z. Mo, Antibacterial characteristics and mechanisms of ε-poly-lysine against *Escherichia coli* and *Staphylococcus aureus*. *Food Control* **43**, 22–27 (2014).

23. M. Hosoya, J. Neyts, N. Yamamoto, D. Schols, R. Smoeck, R. Pauwels, E. de Clercq, Inhibitory effects of polycations on the replication of enveloped viruses (HIV, HSV, CMV, RSV, influenza A virus and togaviruses) in vitro. *Antivir. Chem. Chemother.* **2**, 243–248 (1991).

24. N. Langeland, L. J. Moore, H. Holmsen, L. Haarr, Interaction of polylysine with the cellular receptor for herpes simplex virus type 1. *J. Gen. Virol.* **69**, 1137–1145 (1988).

25. B. Binks, S. Lumsdon, Pickering emulsions stabilized by monodisperse latex particles: Effects of particle size. *Langmuir* **17**, 4540–4547 (2001).

26. K. J. Bretz, Á. Jobbagy, K. Bretz, Force measurement of hand and fingers. *Biomech. Hung.* **3**, 61–66 (2010).

27. M. J. Hessert, M. Vyas, J. Leach, K. Hu, L. A. Lipsitz, V. Novak, Foot pressure distribution during walking in young and old adults. *BMC Geriatr.* **5**, 8 (2005).

28. S. Liu, D. S. Shah, R. Kramer-Bottiglio, Highly stretchable multilayer electronic circuits using biphasic gallium-indium. *Nat. Mater.* **20**, 851–858 (2021).

29. M. H. Malakooti, N. Kazem, J. Yan, C. Pan, E. J. Markvicka, K. Matyjaszewski, C. Majidi, Liquid metal supercooling for low-temperature thermoelectric wearables. *Adv. Funct. Mater.* **29**, 1906098 (2019).

30. T. Someya, M. Amagai, Toward a new generation of smart skins. *Nat. Biotechnol.* **37**, 382–388 (2019).

31. S. Chao, Y. Li, R. Zhao, L. Zhang, Y. Li, C. Wang, X. Li, Synthesis and characterization of tigecycline-loaded sericin/poly (vinyl alcohol) composite fibers via electrospinning as antibacterial wound dressings. *J. Drug Deliv. Sci. Technol.* **44**, 440–447 (2018).

32. X. Zheng, H. Lee, T. H. Weisgraber, M. Shusteff, J. DeOtte, E. B. Duoss, J. D. Kuntz, M. M. Biener, Q. Ge, J. A. Jackson, S. O. Kucheyev, N. X. Fang, C. M. Spadaccini, Ultralight, ultrastiff mechanical metamaterials. *Science* **344**, 1373–1377 (2014).

33. S. Liu, Y. Rao, H. Jang, P. Tan, N. Lu, Strategies for body-conformable electronics. *Matter* **5**, 1104–1136 (2022).

34. L. Tian, B. Zimmerman, A. Akhtar, K. J. Yu, M. Moore, J. Wu, R. J. Larsen, J. W. Lee, J. Li, Y. Liu, B. Metzger, S. Qu, X. Guo, K. E. Mathewson, J. A. Fan, J. Cornman, M. Fatina, Z. Xie, Y. Ma, J. Zhang, Y. Zhang, F. Dolcos, M. Fabiani, G. Gratton, T. Bretl, L. J. Hargrove, P. V. Braun, Y. Huang, J. A. Rogers, Large-area MRI-compatible epidermal electronic interfaces for prosthetic control and cognitive monitoring. *Nat. Biomed. Eng.* **3**, 194–205 (2019).

35. N. Driscoll, B. Erickson, B. B. Murphy, A. G. Richardson, G. Robbins, N. V. Apollo, G. Mentzelopoulos, T. Mathis, K. Hantanasirisakul, P. Bagga, S. E. Gullbrand, M. Sergison, R. Reddy, J. A. Wolf, H. I. Chen, T. H. Lucas, T. R. Dillingham, K. A. Davis, Y. Gogotsi, J. D. Medaglia, F. Vitale, MXene-infused bioelectronic interfaces for multiscale electrophysiology and stimulation. *Sci. Transl. Med.* **13**, eabf8629 (2021).

36. J. F. Schenck, The role of magnetic susceptibility in magnetic resonance imaging: MRI magnetic compatibility of the first and second kinds. *Med. Phys.* **23**, 815–850 (1996).

37. A. L. Byrd, Y. Belkaid, J. A. Segre, The human skin microbiome. *Nat. Rev. Microbiol.* **16**, 143–155 (2018).

38. Y. Su, Z. Zhi, Q. Gao, M. Xie, M. Yu, B. Lei, P. Li, P. X. Ma, Autoclaving-derived surface coating with in vitro and in vivo antimicrobial and antibiofilm efficacies. *Adv. Healthc. Mater.* **6**, 1601173 (2017).

39. J.-H. Kim, S. Kim, J.-H. So, K. Kim, H.-J. Koo, Cytotoxicity of gallium–indium liquid metal in an aqueous environment. *ACS Appl. Mater. Interfaces* **10**, 17448–17454 (2018).

40. A. J. Bandodkar, V. W. S. Hung, W. Jia, G. Valdés-Ramírez, J. R. Windmiller, A. G. Martinez, J. Ramírez, G. Chan, K. Kerman, J. Wang, Tattoo-based potentiometric ion-selective sensors for epidermal pH monitoring. *Analyst* **138**, 123–128 (2013).

41. H. U. Chung, B. H. Kim, J. Y. Lee, J. Lee, Z. Xie, E. M. Ibler, K.H. Lee, A. Banks, J. Y. Jeong, J. Kim, C. Ogle, D. Grande, Y. Yu, H. Jang, P. Assem, D. Ryu, J. W. Kwak, M. Namkoong, J. B. Park, Y. Lee, D. H. Kim, A. Ryu, J. Jeong, K. You, B. Ji, Z. Liu, Q. Huo, X. Feng, Y. Deng, Y. Xu, K.I. Jang, J. Kim, Y. Zhang, R. Ghaffari, C. M. Rand, M. Schau, A. Hamvas, D. E. Weese-Mayer, Y. Huang, S. M. Lee, C. H. Lee, N. R. Shanbhag, A. S. Paller, S. Xu, J. A. Rogers, Binodal, wireless epidermal electronic systems with in-sensor analytics for neonatal intensive care. *Science* **363**, eaau0780 (2019).

42. Y. Yu, J. Nassar, C. Xu, J. Min, Y. Yang, A. Dai, R. Doshi, A. Huang, Y. Song, R. Gehlhar, A.D. Ames, W. Gao, Biofuel-powered soft electronic skin with multiplexed and wireless sensing for human-machine interfaces. *Sci. Robot.* **5**, eaaz7946 (2020).

43. M. P. Turakhia, D. D. Hoang, P. Zimetbaum, J. D. Miller, V. F. Froelicher, U. N. Kumar, X. Xu, F. Yang, P. A. Heidenreich, Diagnostic utility of a novel leadless arrhythmia monitoring device. *Am. J. Cardiol.* **112**, 520–524 (2013).

44. Z. I. Attia, S. Kapa, F. Lopez-Jimenez, P. M. McKie, D. J. Ladewig, G. Satam, P. A. Pellikka, M. Enriquez-Sarano, P. A. Noseworthy, T. M. Munger, S. J. Asirvatham, C. G.

Scott, R. E. Carter, P. A. Friedman, Screening for cardiac contractile dysfunction using an artificial intelligence–enabled electrocardiogram. *Nat. Med.* **25**, 70–74 (2019).

45. S. Mansouri, T. Alhadidi, S. Chabchoub, R. B. Salah, Impedance cardiography: Recent applications and developments. *Biomed. Res.* **29**, 3542–3552 (2018).

46. D. Naranjo-Hernández, J. Reina-Tosina, M. Min, Fundamentals, recent advances, and future challenges in bioimpedance devices for healthcare applications. *J. Sens.* **2019**, 9210258 (2019).

47. Y. Xie, R. Song, D. Yang, H. Yu, C. Sun, Q. Xie, R. X. Xu, Motion robust ICG measurements using a two-step spectrum denoising method. *Physiol. Meas.* **42**, 095004 (2021).

48. K. Ushimaru, Y. Hamano, H. Katano, Antimicrobial activity of ε-poly-L-lysine after forming a water-insoluble complex with an anionic surfactant. *Biomacromolecules* **18**, 1387–1392 (2017).

49. H.-W. Zhu, H. L. Gao, H. Y. Zhao, J. Ge, B. C. Hu, J. Huang, S. H. Yu, Printable elastic silver nanowire-based conductor for washable electronic textiles. *Nano Res.* **13**, 2879–2884 (2020).

50. P. Li, Y. F. Poon, W. Li, H. Y. Zhu, S. H. Yeap, Y. Cao, X. Qi, C. Zhou, M. Lamrani, R. W. Beuerman, E. T. Kang, Y. Mu, C. M. Li, M. W. Chang, S. S. Jan Leong, M. B. Chan-Park, A polycationic antimicrobial and biocompatible hydrogel with microbe membrane suctioning ability. *Nat. Mater.* **10**, 149–156 (2011).

51. C. Lei, J. Yang, J. Hu, X. Sun, On the calculation of $TCID_{50}$ for quantitation of virus infectivity. *Virol. Sin.* **36**, 141–144 (2021).

52. Y. Khan, M. L. Mauriello, P. Nowruzi, A. Motani, G. Hon, N. Vitale, J. Li, J. Kim, A. Foudeh, D. Duvio, E. Shols, M. Chesnut, J. Landay, J. Liphardt, L. Williams, K. D. Sudheimer, B. Murmann, Z. Bao, P. E. Paredes, Design considerations of a wearable electronic-skin for mental health and wellness: Balancing biosignals and human factors.

bioRxiv 2021.01.20.427496 [**Preprint**]. 21 January 2021. https://doi.org/10.1101/2021.01.20.427496.

53. N. Cohen, K. Bhattacharya, A numerical study of the electromechanical response of liquid metal embedded elastomers. *Int. J. Non-Linear Mech.* **108**, 81–86 (2019).

54. M. Geerligs, L. van Breemen, G. Peters, P. Ackermans, F. Baaijens, C. Oomens, In vitro indentation to determine the mechanical properties of epidermis. *J. Biomech.* **44**, 1176–1181 (2011).

55. M. L. Crichton, B. C. Donose, X. Chen, A. P. Raphael, H. Huang, M. A. F. Kendall, The viscoelastic, hyperelastic and scale dependent behaviour of freshly excised individual skin layers. *Biomaterials* **32**, 4670–4681 (2011).